Model-Based Calibration of Transmission Test Bench Controls for Hardware-in-the-Loop Applications

Metadata of the chapter that will be visualized in SpringerLink

Book Title	Advances in Engine and Powertrain Research and Technology
Series Title	
Chapter Title	Model-Based Calibration of Transmission Test Bench Controls for Hardware-in-the-Loop Applications
Copyright Year	2022
Copyright HolderName	The Author(s), under exclusive license to Springer Nature Switzerland AG

Corresponding Author	Family Name	**Galvagno**
	Particle	
	Given Name	**Enrico**
	Prefix	
	Suffix	
	Role	
	Division	
	Organization	Politecnico Di Torino
	Address	10129, Turin, Italy
	Email	enrico.galvagno@polito.it
	ORCID	https://orcid.org/0000-0003-2558-8798
Author	Family Name	**Tota**
	Particle	
	Given Name	**Antonio**
	Prefix	
	Suffix	
	Role	
	Division	
	Organization	Politecnico Di Torino
	Address	10129, Turin, Italy
	Email	antonio.tota@polito.it
	ORCID	https://orcid.org/0000-0002-7151-8873
Author	Family Name	**Mari**
	Particle	
	Given Name	**Gianluca**
	Prefix	
	Suffix	
	Role	
	Division	
	Organization	Politecnico Di Torino
	Address	10129, Turin, Italy
	Email	gianluca.mari@polito.it
Author	Family Name	**Velardocchia**
	Particle	
	Given Name	**Mauro**

Prefix	
Suffix	
Role	
Division	
Organization	Politecnico Di Torino
Address	10129, Turin, Italy
Email	mauro.velardocchia@polito.it
ORCID	https://orcid.org/0000-0003-0757-1626

Abstract	Hardware in the loop test rigs represent one of the most adopted experimental platforms to assess automotive transmissions dynamic performances. Even if their architectures may range among few different configurations, they share general requirements from the mechanical design to their controller implementation for a real-time deployment. This chapter is focused on a real application of a Dual Clutch Transmission Hardware in the Loop test rig. Two electric motors are installed to emulate the effect of the Internal Combustion Engine to the transmission input and the vehicle motion resistances to the transmission output, respectively. For a proper Hardware in the Loop operation, if a torque control is selected for one electric motor, the second one requires to be controlled in speed. Moreover, the controls structure cannot be usually customized since they are conventionally constrained by industrial drive limitations. This chapter includes an accurate analysis of the reciprocal influence of the two controllers since they are mechanically applied to the input and output of the same transmission. The analysis is further supported by a linear model of the transmission test rig which is able to predict the sensitivity effect of the two controller's activation on the test rig performance. An optimal tuning of the two controllers' parameters is then described to achieve the desired level of reference tracking and disturbance rejection targets.

Keywords (separated by '-')	Dynamic modelling - HiL testing - Experimental model validation - Transmission test bench - Control calibration - Frequency response functions - AC motors speed and torque control tuning - Torsional vibrations

Model-Based Calibration of Transmission Test Bench Controls for Hardware-in-the-Loop Applications

Enrico Galvagno, Antonio Tota, Gianluca Mari, and Mauro Velardocchia

Abstract Hardware in the loop test rigs represent one of the most adopted experimental platforms to assess automotive transmissions dynamic performances. Even if their architectures may range among few different configurations, they share general requirements from the mechanical design to their controller implementation for a real-time deployment. This chapter is focused on a real application of a Dual Clutch Transmission Hardware in the Loop test rig. Two electric motors are installed to emulate the effect of the Internal Combustion Engine to the transmission input and the vehicle motion resistances to the transmission output, respectively. For a proper Hardware in the Loop operation, if a torque control is selected for one electric motor, the second one requires to be controlled in speed. Moreover, the controls structure cannot be usually customized since they are conventionally constrained by industrial drive limitations. This chapter includes an accurate analysis of the reciprocal influence of the two controllers since they are mechanically applied to the input and output of the same transmission. The analysis is further supported by a linear model of the transmission test rig which is able to predict the sensitivity effect of the two controller's activation on the test rig performance. An optimal tuning of the two controllers' parameters is then described to achieve the desired level of reference tracking and disturbance rejection targets.

Keywords Dynamic modelling · HiL testing · Experimental model validation · Transmission test bench · Control calibration · Frequency response functions · AC motors speed and torque control tuning · Torsional vibrations

E. Galvagno (✉) · A. Tota · G. Mari · M. Velardocchia
Politecnico Di Torino, 10129 Turin, Italy
e-mail: enrico.galvagno@polito.it

A. Tota
e-mail: antonio.tota@polito.it

G. Mari
e-mail: gianluca.mari@polito.it

M. Velardocchia
e-mail: mauro.velardocchia@polito.it

T. Parikyan (ed.), *Advances in Engine and Powertrain Research and Technology*, Mechanisms and Machine Science 114,
https://doi.org/10.1007/978-3-030-91869-9_13

509827_1_En_13_Chapter ☑ TYPESET ☐ DISK ☐ LE ☑ CP Disp.:13/1/2022 Pages: 34 Layout: T1-Standard

1 Introduction

Automotive transmission systems are designed to comply with strict functionality, reliability, and safety requirements to meet the desired vehicle drivability performance [1]. Usually, carmakers face the transmission development process through extensive experimental campaigns carried out to evaluate the transmission performance. A complete experimental set-up would require the connection of the transmission system to the internal combustion engine (ICE) or its direct installation on board the vehicle to reproduce with high fidelity the working operating conditions. However, this solution presents a considerable number of drawbacks in terms of costs and maintenance services that an ICE or a full vehicle system would implicate. Therefore, a more convenient solution involves the introduction of one or more electric motors to emulate the steady-state and the dynamic characteristics of the ICE as well as the load condition imposed by the vehicle motion resistances [2]. In this regard, Hardware-In-the-Loop (HiL) test benches have been very popular due to their advantages in terms of cost, flexibility, repeatability, and test automation since they adopt a model-based approach with a mix of real and emulated sensors, actuators, and vehicle subsystems to meet the cost and time constraints. HiL can reduce the testing effort up to a 90% if compared to the conventional driving test procedures, as described in [3]. Furthermore, HiL test benches have been widely used in the automotive industry to study the behavior of physical vehicle components and subsystems, e.g. the dual mass flywheel influence on transmission dynamics in [4], or to design and validate electronic control units. For example, a HiL simulation has been developed in [5, 6] for testing active brake control strategies such the Anti-lock Brake System (ABS), the Traction Control System (TCS), and the Electronic Stability Program (ESP). A similar application is also presented in [7–9], where a continuous braking pressure control strategy is implemented and validated on a HiL test rig with a conventional passenger car braking system. In [10] a HiL system is set-up for the development process of an electronic steering device to guarantee repetitive simulations and to demonstrate the efficacy with respect to on-board vehicle testing sessions. Finally, it is also convenient to integrate two or more HiL test rigs for evaluating their mutual influence, as also described by [11] where a DCT and a brake HiL systems are coupled to enhance the transmission Noise, Vibrations, Harshness (NVH) performance.

The activity described in this paper presents a real application of a DCT HiL test rig available at the Politecnico di Torino. Two electric motors are installed to emulate the effect of the ICE to the transmission input and the vehicle motion resistances to the transmission output, respectively. The control units of the electric motors adopted for HiL purposes, are usually designed with a rigid structure, typically a Proportional Integral Derivative (PID) logic, that is conventionally constrained by industrial drive limitations. The main contribution of the paper is to provide a model-based approach for analyzing and tuning the interaction between the control of the two electric motors. The torsional dynamics of the driveline installed on the test bench is simulated through a 6-degree-of-freedom (DOF) lumped parameter model, that represents an extended version of the 5-DOF model proposed in [12]. The transmission model is also enhanced by considering the closed-loop dynamics introduced by the PID algorithm for regulating the speed of one electric motor. An extensive sensitivity analysis of the model to the mechanical and control parameters is proposed to evaluate their effect on the controller reference speed tracking performance and on its disturbance rejection against the torque applied by the second electric motor. Then, the tuned speed control strategy is experimentally validated on the DCT HiL test rig.

The manuscript is organized as follows: Sect. 2 provides an overview of the hardware and software available on the DCT HiL test rig; Sect. 3 introduces the transmission model, and analyze the dynamic behavior of both open-loop and closed-loop configurations; Sect. 4 presents the sensitivity analysis of the linear model to the mechanical and control parameters, while Sect. 5 covers the experimental validation, both in frequency and time domain, of the proposed methodology; finally, conclusions are drawn in Sect. 6.

2 Transmission HiL Test Rig: Hardware (HW) and Software (SW)

The test bench here presented is meant to be used as a HiL system for automotive transmission testing. The typical loading condition associated with the usage of a mechanical transmission on a real car can be reproduced. To this aim, a simulation model running and exchanging in real time signals with sensors and actuators is implemented. Some examples of test benches sharing a similar HiL technology are reported in [13, 14]. A detailed description of the hardware and software components is given in the next two sections.

2.1 Hardware Components

Figure 1 shows a picture of the HiL transmission test bench in the Mechanical Laboratory of Politecnico di Torino. It features two electric motors (M1 and M2) and two transmissions, the first is a Dual Clutch Transmission (DCT), that is the system under investigation, and the second a Manual Transmission (MT).

As visible in Fig. 2, the connection between the two transmissions is realized through the two output shafts SA1 and SA2, i.e. the original left half shafts of the two drivelines, and a brake disk D.

More specifically, the main subsystems that are visible in Fig. 1 are commented below (starting from the left part of the picture):

(i) M1: a 37 kW 2-pole 3-phase induction motor featuring a nominal torque of 121 Nm and a nominal speed of 2920 rpm. It is operated in the four quadrants of the torque-speed plane by an inverter with a torque overload capacity of 150%. For this application, the “torque-control with speed limitation” mode

509827_1_En_13_Chapter ✓ TYPESET DISK LE ✓ CP Disp.:13/1/2022 Pages: 34 Layout: T1-Standard

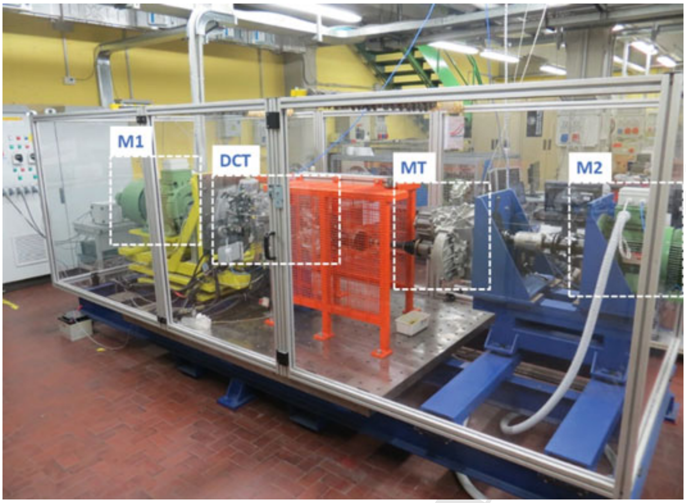

Fig. 1 Transmission test bench in the Mechanical Laboratory of Politecnico di Torino

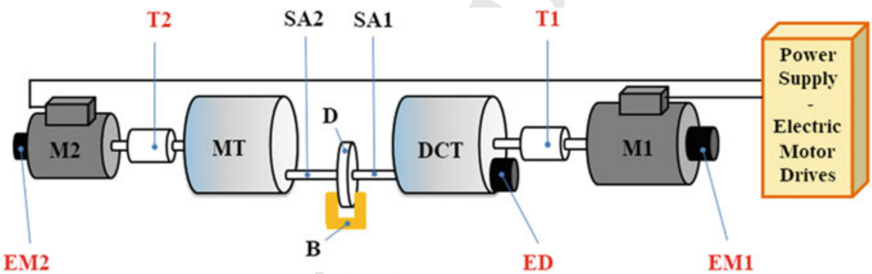

Fig. 2 Layout of the transmission test bench: electric motors (M1, M2), speed sensors (encoders EM1, EM2 and ED), torque sensors (T1, T2), disk (D), brake (B) and half shafts (SA1, SA2)

is selected for reproducing the torque delivered by the internal combustion engine of the car.

(ii) DCT: a 6-speed dry Dual Clutch Transmission (see, e.g., [15] for the kinematic and dynamic ehavior of this transmission).

(iii) MT: a 6-speed Manual Transmission with one primary and two secondary shafts;

(iv) M2: a 11 kW 6-pole 3-phase induction motor with a nominal torque of 110 Nm and a nominal speed of 955 rpm. It is powered by an inverter with 150% torque overload capacity which allows the electric machine operating in four quadrants. For this application, the "encoder feedback speed-control" mode is selected and is used to simulate the vehicle load at the output shaft of the DCT, that is due to the aerodynamic and rolling resistance, the road slope, and the vehicle inertial effects.

To monitor the actual dynamic state of the transmission system, the test bench is equipped with a number of sensors that are here reported.

(i) Two torque-meters (T1 and T2 in Fig. 2), measuring the torque provided by the two electric motors: T1 torque meter, is particularly suitable for dynamic torque measurements having a bandwidth of 3 kHz and a maximum torque of 500 Nm; T2 is a torque meter with an integrated tachometer, capable of withstanding dynamic torques of 226 Nm.
(ii) Three rotary incremental encoders: EM1 and EM2 measure the angular position and speed of the two motors while ED measures the position and speed of the DCT differential; the number of pulses per revolution of the three sensors are 1024, 4096 and 9600 respectively. It is worth noting that encoders EM1 and EM2 are the same sensors used by the electric drives for implementing the closed-loop speed control of the two motors.
(iii) Magnetic pickup sensors for monitoring the angular speed of the components inside the DCT, they are positioned: on the secondary mass of the dual mass flywheel, on the differential crown, on the two differential pinions (lower and upper secondary shaft), on the first and third gear on the lower secondary shaft and on the second and fourth gear on the upper secondary shaft.
(iv) Two thermocouples are also mounted on the DCT, one for measuring the temperature of the lubricating oil and the other one for monitoring the temperature of the hydraulic fluid of the actuation system.
(v) A triaxial accelerometer on the gearbox housing and a microphone for further NVH analysis, e.g. gearshift noise and vibration.

The two electric motors are operated by means of electric drives, the 37 and 11 kW inverters shown in Fig. 3, which allow controlling either the actual torque or the speed in open or closed-loop, the latter through PID controllers, depending on the user's choice. Both the drives are set for operating with vector control method.

The electric cabinet of the test rig also include an Active Front End (AFE) which connects the two inverters via a direct current (DC) bus, allowing an efficient power exchange between the two motor drives. AFE may absorb or give back to the electric grid the net electric power deriving from the specific operating condition of the bench. Power regeneration is therefore enabled through this system architecture,

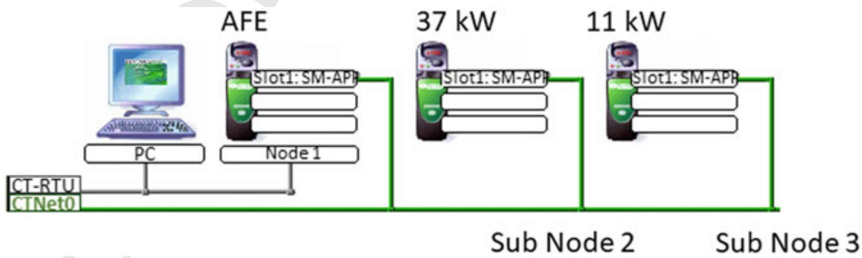

Fig. 3 Communication network between the electric drives (37 and 11 kW) and the active front end (AFE)

thus avoiding the dissipation, e.g. on braking resistors, the negative electric power. For closed-loop control, the microcontrollers inside the electrical cabinet use the information from the torque transducers and the encoders mounted on the bench. The front panel of the electrical cabinet features displays for manual settings of the motor drives and many connectors for analog and digital I/O, Controller Area Network (CAN) and Ethernet communication for real-time control of the test bench and for remote monitoring and programming the inverter parameters.

It is worth underlining that a good controllability of both electric motors in terms of torque and speed reference tracking performance is mandatory for such kind of test bench. The optimization of the available parameters, in particular the PID gains of the feedback controllers, is crucial for obtaining a satisfactory trade-off between the conflicting requirements, i.e. high dynamic performance, low control effort and low noise and vibrations. The step change of some system parameters during the normal working condition of the bench, i.e. the gear ratio of the two transmissions, leads to different optimal parameter sets for different test bench configurations. This last specific characteristic requires specific analysis and considerations that are the aim of this paper.

2.2 Software Components

The HiL testing methodology requires modelling the dynamics of all the systems interacting with the transmission under test that are present on a real car, but that are not physically installed on the bench. Figure 4 highlights the main interactions between hardware and software components of the test bench. In the central part of the picture are the two models for engine and vehicle simulation, on the left the inputs signals from the Transmission Control Unit (TCU) via CAN, from encoder and torque sensors, while on the right the output signals for the TCU, the torque and the speed setpoints for the controllers of the two motors.

Suitable models for the internal combustion engine and for the vehicle longitudinal dynamics simulation must be developed and implemented in the HiL software.

Vehicle dynamics model

A 1 degree of freedom model for the vehicle longitudinal dynamics is normally adequate for the present application, in which the pure rolling condition for the tires is assumed. The model must account for the motion resistance due to aerodynamics, rolling and road slope and for the inertial effects of the vehicle. This block computes the reference speed for M2 motor according to the torque applied by the powertrain and measured by T2 torque sensors and the actual speed of M2 motor.

Engine model

The engine model must include the following functions to accomplish the tasks required by HiL transmission testing for conventional powertrains: starter simulation, engine cut-off during accelerator pedal release, redline control for maximum speed

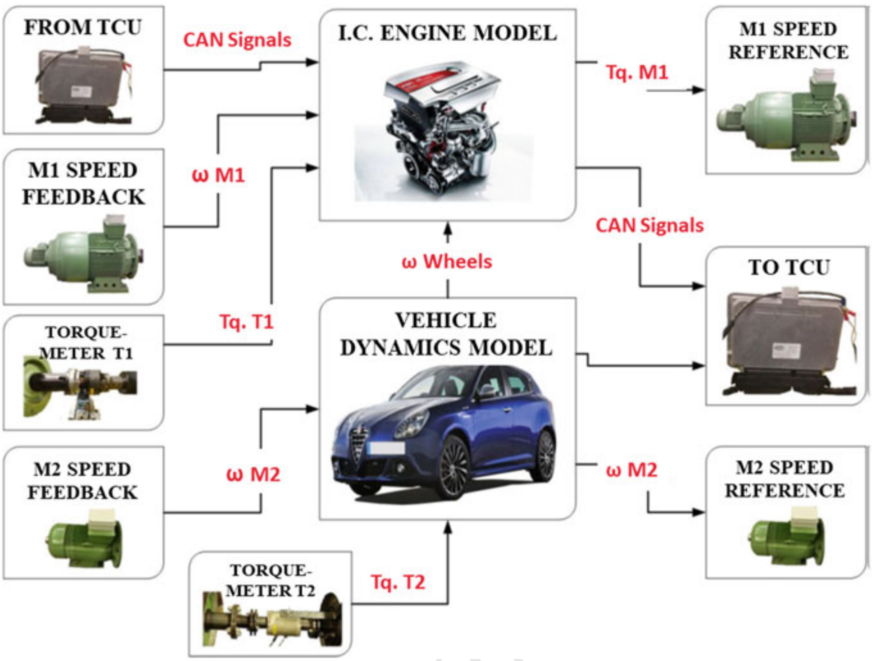

Fig. 4 HiL software scheme: on the left) the inputs from the TCU and the torque and speed sensors of the electric motors, in the middle) the main simulation blocks, on the right) the output setpoints for the electric motors and the signals for the TCU

limitation, idle speed control, torque saturation according to engine maximum and minimum torque map, combustion delay and turbo lag to account for the delay introduced by the gasoline or diesel engine torque generation system. Figure 5 shows a block diagram of the engine model, in which the said functions are reported; this model computes the torque delivered by the virtual ICE according to the actual working condition of the bench. The engine torque signal becomes a reference for the torque control of M1 motor and is sent via CAN to the corresponding drive.

Typical examples of experiments carried out on the test bench include: vehicle start-up, gear shift, engine start and stop, accelerator pedal tip-in/tip-out, run-up and coast-down, acceleration and deceleration with upshifts and downshifts. This test bench was also recently used to study the integration with other active chassis systems with the aim of enhancing the transmission NVH performance.

3 System Model and Analysis

The DCT torsional dynamics is investigated through a six-degree-of-freedom (DOF) lumped parameter model, as shown in Fig. 6.

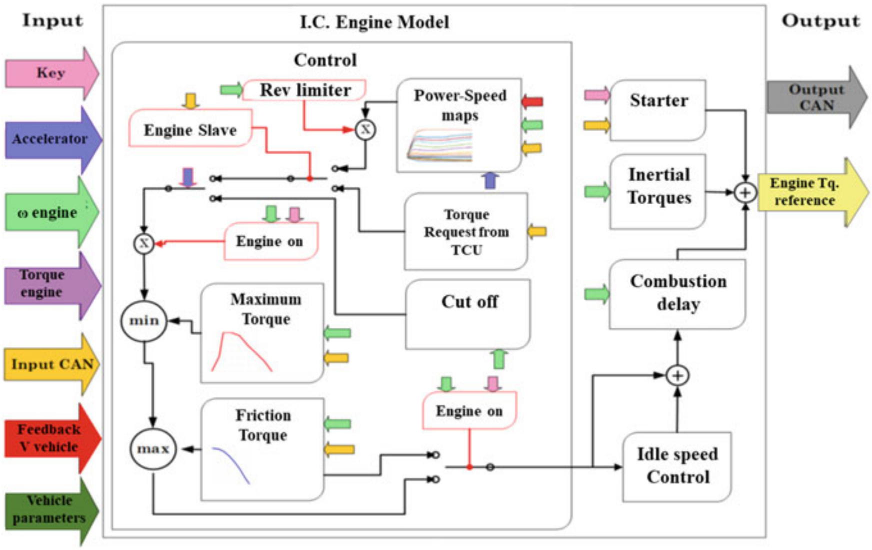

Fig. 5 ICE model block diagram. The colours of the arrow are used to identify which input enters in each single blocks from the central part of the picture

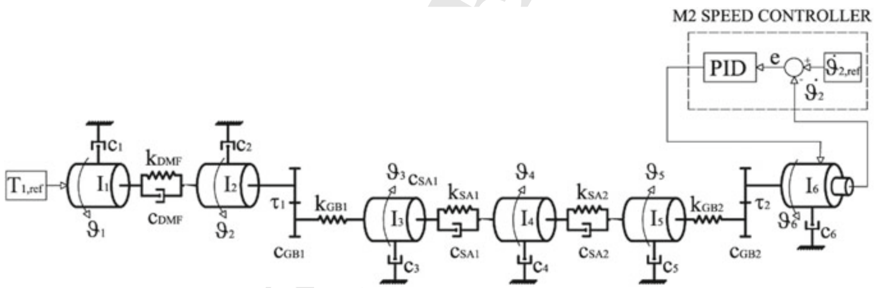

Fig. 6 Schematic of the torsional model of the transmission test bench

The test bench torsional model includes the following elements:

- The Dual Mass Flywheel (DMF) is modelled with two inertial components, I_1 and I_2, linked by a low stiffness spring k_{DMF} and a viscous damper with damping coefficient c_{DMF}. The moment of inertia I_1 includes the first DMF mass and the M1 motor inertia, meanwhile the second DMF mass and the equivalent inertia of the DCT gearbox (except its differential inertia I_3) are integrated in I_2.
- The DCT gearbox model account for the actual gear ratio τ_1 (defined as the ratio between the input and output speeds) and an equivalent torsional stiffness k_{GB1} at the transmission output shaft. The value of k_{GB1} varies with the gear ratio τ_1 due to the variation of the portion of the shaft through which the power is transmitted when the different gears are engaged.

- The MT gearbox is modelled with the actual gear ratio τ_2 and an equivalent stiffness k_{GB2} (evaluated at its output shaft) between differential inertia I_5 and inertia I_6 which includes the M2 mass moment of inertia and the equivalent inertia of the MT gearbox.
- The inertia of the brake disk I_4 connecting the DCT and MT output shafts through the two half shafts SA1 and SA2, respectively, which are modelled as a pair of spring damper elements.

The values of the said parameters used to define the transmission test bench model are reported in Table 1. While inertial and elastic parameters can be quite accurately derived from component technical drawing or data sheet, damping cannot be easily evaluated; therefore a curve fitting method based on the comparison of the simulated and experimental frequency response functions (FRFs) (see Sect. 3.3 for further information) was set up to identify the viscous damping parameters of the model.

As already mentioned in the former section, the electric motor M1 is usually set to apply a desired torque to emulate the steady-state torsional behavior of the ICE engine meanwhile the motor M2 is controlled in speed to replicate the vehicle longitudinal dynamics through the mathematical model of the motion resistance.

The system analysis is conducted in two steps that will be called.

(a) *open-loop system* if the two motors M1 and M2 apply torque to the mechanical system without using any feedback signals from the test rig.

(b) *closed-loop system* if M2 is speed controlled using feedback from EM1 sensor and M1 applies torque to the mechanical system without feedback.

3.1 Open-Loop System Equations

The equations of motion of the torsional model depicted in Fig. 6 are:

$$
\begin{aligned}
I_1\ddot{\vartheta}_1 + c_{DMF}(\dot{\vartheta}_1 - \dot{\vartheta}_2) + c_1\dot{\vartheta}_1 + k_{DMF}(\vartheta_1 - \vartheta_2) &= T_1 \\
I_2\ddot{\vartheta}_2 + \left(c_2 + \frac{c_{GB1}}{\tau_1^2}\right)\dot{\vartheta}_2 - c_{DMF}(\dot{\vartheta}_1 - \dot{\vartheta}_2) - \frac{k_{GB1}}{\tau_1}\left(\vartheta_3 - \frac{\vartheta_2}{\tau_1}\right) - k_{DMF}(\vartheta_1 - \vartheta_2) &= 0 \\
I_3\ddot{\vartheta}_3 + c_3\dot{\vartheta}_3 + c_{SA1}(\dot{\vartheta}_3 - \dot{\vartheta}_4) + k_{GB1}\left(\vartheta_3 - \frac{\vartheta_2}{\tau_1}\right) + k_{SA1}(\vartheta_3 - \vartheta_4) &= 0 \\
I_4\ddot{\vartheta}_4 + c_4\dot{\vartheta}_4 + c_{SA1}(\dot{\vartheta}_4 - \dot{\vartheta}_3) + c_{SA2}(\dot{\vartheta}_4 - \dot{\vartheta}_5) + k_{SA1}(\vartheta_4 - \vartheta_3) + k_{SA2}(\vartheta_4 - \vartheta_5) &= 0 \\
I_5\ddot{\vartheta}_5 + c_5\dot{\vartheta}_5 + c_{SA2}(\dot{\vartheta}_5 - \dot{\vartheta}_4) + k_{GB2}\left(\vartheta_5 - \frac{\vartheta_6}{\tau_2}\right) + k_{SA2}(\vartheta_5 - \vartheta_4) &= 0 \\
I_6\ddot{\vartheta}_6 + \left(c_6 + \frac{c_{GB2}}{\tau_2^2}\right)\dot{\vartheta}_6 - \frac{k_{GB2}}{\tau_2}\left(\vartheta_5 - \frac{\vartheta_6}{\tau_2}\right) &= T_6
\end{aligned}
\tag{1}
$$

where $\tau_1 = \tau_{G1}\tau_{F1}$, $\tau_2 = \tau_{G2}\tau_{F2}$ and the generalized coordinates are the angular positions of each inertial component in Fig. 6: $\boldsymbol{q} = \{\vartheta_1\vartheta_2\vartheta_3\vartheta_4\vartheta_5\vartheta_6\}^T$, and T_1 and T_6 represent the torques applied by M1 and M2, respectively.

Table 1 Parameters of the transmission test bench model

Quantity	Symbol	Value	Units
Primary DMF inertia	I_1	0.195	kgm^2
Secondary DMF inertia	I_2	0.147	kgm^2
DCT inertia (at output shaft)	I_3	0.123	kgm^2
Brake disk inertia	I_4	0.18	kgm^2
MT differential inertia	I_5	0.172	kgm^2
MT and M2 inertia	I_6	0.069	kgm^2
DCT gear ratio	τ_{G1}	$[4.15, 2.27, 1.43, 0.98, 0.76, 0.62, -4]$	–
MT gear ratio	τ_{G2}	$[4.17, 2.35, 1.46, 0.95, 0.69, 0.55, -4.08]$	–
DCT final drive ratio	τ_{F1}	4.118	–
MT final drive ratio	τ_{F2}	4.222	–
Fly-wheel stiffness	k_{DMF}	458.4	Nm/rad
DCT stiffness	k_{GB1}	$[2.73, 7.84, 0.96, 3.78, 0.33, 1.82] \times 10^5$	Nm/rad
MT stiffness	k_{GB2}	1.34×10^5	Nm/rad
First driveshaft stiffness	k_{SA1}	0.12×10^5	Nm/rad
Second driveshaft stiffness	k_{SA2}	0.15×10^5	Nm/rad
DOF damping	$[c_1, c_2, \ldots, c_6]$	$[0.2, 2, 0.02, 0.34, 4, 0]$	Nms/rad
DMF Damping	c_{DMF}	7.5	Nms/rad
DCT damping	c_{GB1}	0	Nms/rad
MT damping	c_{GB2}	4	Nms/rad
First driveshaft damping	c_{SA1}	0.1	Nms/rad
Second driveshaft damping	c_{SA2}	0.1	Nms/rad

Equation (1) can be expressed with the following matrix formulation:

$$\boldsymbol{M}\ddot{\boldsymbol{q}} + \boldsymbol{C}\dot{\boldsymbol{q}} + \boldsymbol{K}\boldsymbol{q} = \underbrace{\begin{bmatrix} 1 & 0 \\ 0 & 0 \\ 0 & 0 \\ 0 & 0 \\ 0 & 0 \\ 0 & 1 \end{bmatrix}}_{\boldsymbol{E}} \begin{bmatrix} T_1 \\ T_6 \end{bmatrix} \tag{2}$$

where the mass matrix $\boldsymbol{M}$, the damping matrix $\boldsymbol{C}$ and the stiffness matrix $\boldsymbol{K}$ are defined as:

$$\begin{gathered}
\boldsymbol{M} = diag(I_1, I_2, I_3, I_4, I_5, I_6) \\
\boldsymbol{C} = \begin{bmatrix} c_{DMF} + c_1 & -c_{DMF} & 0 & 0 & 0 & 0 \\ -c_{DMF} & c_{DMF} + c_2 + \frac{c_{GB1}}{\tau_1^2} & 0 & 0 & 0 & 0 \\ 0 & 0 & c_3 + c_{SA1} & -c_{SA1} & 0 & 0 \\ 0 & 0 & -c_{SA1} & c_{SA1} + c_4 + c_{SA2} & -c_{SA2} & 0 \\ 0 & 0 & 0 & -c_{SA2} & c_5 + c_{SA2} & 0 \\ 0 & 0 & 0 & 0 & 0 & c_6 + \frac{c_{GB2}}{\tau_2^2} \end{bmatrix} \\
\boldsymbol{K} = \begin{bmatrix} k_{DMF} & -k_{DMF} & 0 & 0 & 0 & 0 \\ -k_{DMF} & k_{DMF} + \frac{k_{GB1}}{\tau_1^2} & -\frac{k_{GB1}}{\tau_1} & 0 & 0 & 0 \\ 0 & -\frac{k_{GB1}}{\tau_1} & k_{GB1} + k_{SA1} & -k_{SA1} & 0 & 0 \\ 0 & 0 & -k_{SA1} & k_{SA1} + k_{SA2} & -k_{SA2} & 0 \\ 0 & 0 & 0 & -k_{SA2} & k_{SA2} + k_{GB2} & -\frac{k_{GB2}}{\tau_2} \\ 0 & 0 & 0 & 0 & -\frac{k_{GB2}}{\tau_2} & \frac{k_{GB2}}{\tau_2^2} \end{bmatrix}
\end{gathered} \tag{3}$$

The system is then expressed with the state-space representation:

$$\dot{\boldsymbol{x}} = \underbrace{\begin{bmatrix} 0_{6x6} & \boldsymbol{I}_{6x6} \\ -\boldsymbol{M}^{-1}\boldsymbol{K} & -\boldsymbol{M}^{-1}\boldsymbol{C} \end{bmatrix}}_{\boldsymbol{A}_{OL}} x + \underbrace{\begin{bmatrix} 0_{6x2} \\ -\boldsymbol{M}^{-1}\boldsymbol{E} \end{bmatrix}}_{\boldsymbol{B}_{OL}} u \tag{4}$$

where $\boldsymbol{x} = \left\{ \boldsymbol{q} \ \dot{\boldsymbol{q}} \right\}^T$ is the state vector and $\boldsymbol{u} = \left\{ T_1 \ T_6 \right\}^T$ is the input vector.

Modal Analysis

By solving the eigenvalue problem associated with the system in Eq. (4), the damped natural frequency $\omega_{n,r}$, the damping ratio ζ_r, the amplitude and phase of the complex eigenvector $\boldsymbol{\psi_r}$ associated to the r_{th} mode are computed and shown in Figs. 7 and 8 for different values of the MT gears g_2. The eigenvectors are normalized so that

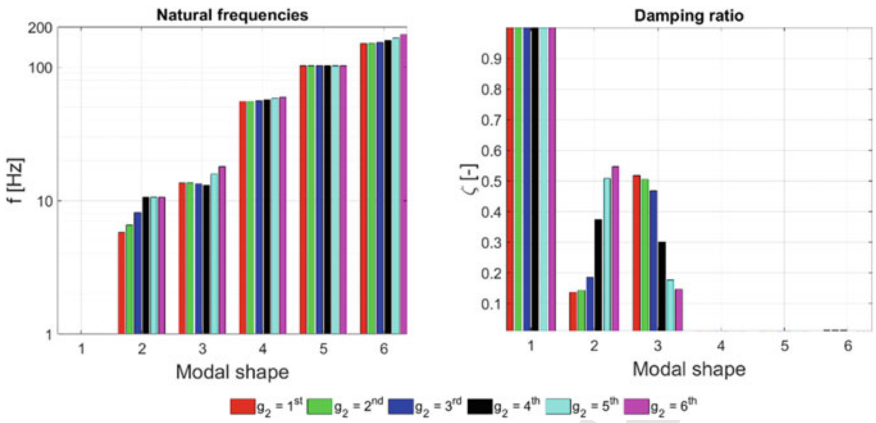

Fig. 7 Natural frequencies and damping ratio of the open-loop system with different MT gears and DCT gear $g_1 = 5th$

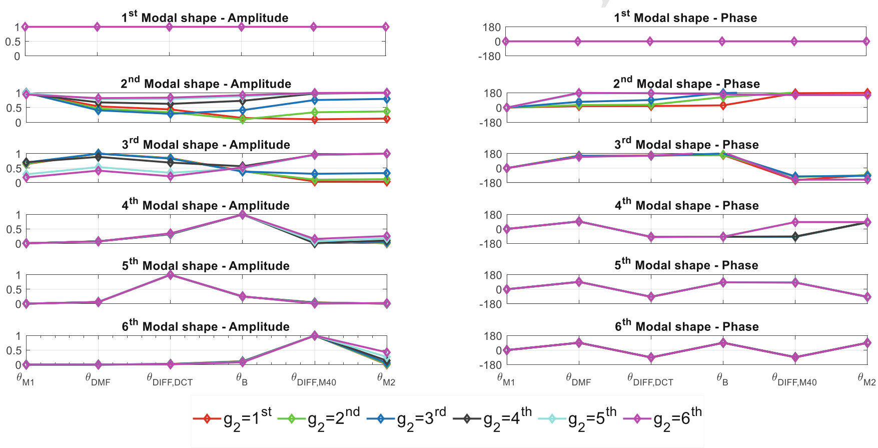

Fig. 8 Modal shape amplitude and phase of the open-loop system with different MT gears and DCT gear $g_1 = 5th$

the modulus of the maximum element is unitary and, due to the presence of the two gear ratios τ_1 and τ_2, they are reduced to the shaft of the electric motor M1. As an example, the r_{th} eigenvector $\boldsymbol{\psi}_{r,M1}$ is scaled as follows:

$$\boldsymbol{\psi}_{r,M1} = \left\{ \psi_1 \;\; \psi_2 \;\; \psi_3\tau_1 \;\; \psi_4\tau_1 \;\; \psi_5\tau_1 \;\; \psi_6\frac{\tau_1}{\tau_2} \right\}_r^T \tag{5}$$

The first mode represents a rigid body mode while the second mode represents the first real torsional mode of the system. The effect of the MT gear ratio mainly influences the second and third modes whereas it does not show a similar influence for higher vibration modes. The last three modes show a very similar characteristic: a single inertia vibrates with respect to the remaining part of the driveline, which stays practically stationary.

A similar sensitivity analysis is conducted for the DCT gear g_1, thus obtaining the results shown in Figs. 9 and 10.

Even in this case, the DCT gear only influences the second and the third modal shapes while higher frequency modes are not affected. Furthermore, the DCT architecture with different torque paths through the transmission, depending on the gear engaged, leads to a non-monotonous trend of the natural frequency with the gear

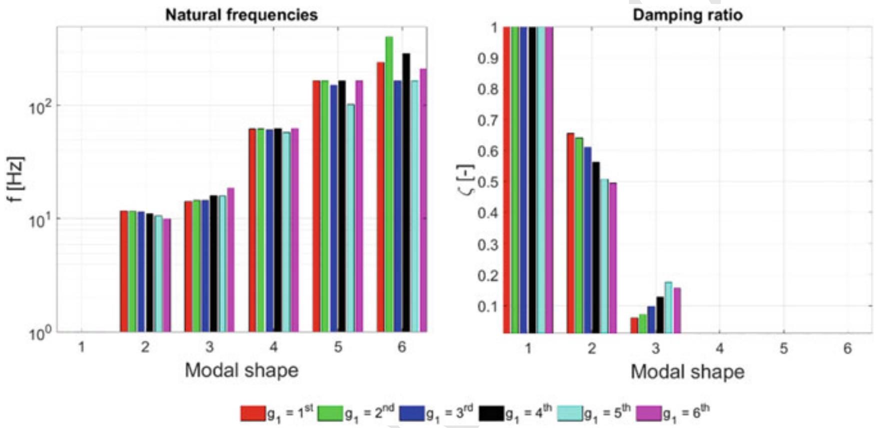

Fig. 9 Natural frequencies and damping ratio of the open-loop system with different DCT gears and MT gear $g_1 = 5th$

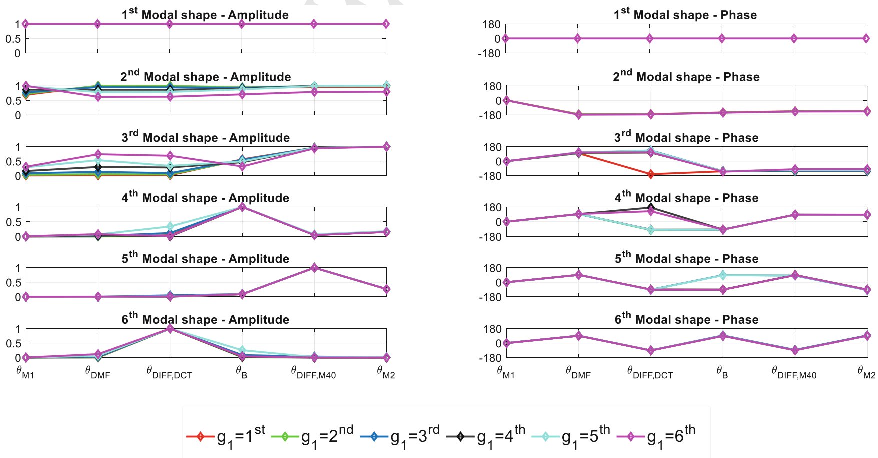

Fig. 10 Modal shape amplitude and phase of the open-loop system with different DCT gears and MT gear $g_1 = 5th$

509827_1_En_13_Chapter ☑ TYPESET ☐ DISK ☐ LE ☑ CP Disp.:13/1/2022 Pages: 34 Layout: T1-Standard

ratio. Indeed, the even and odd gears of DCT are installed on a different input shafts if compared to the MT architecture where each gear is sequentially mounted on the unique input shaft.

3.2 Closed-Loop State-Space Model

The closed-loop system is obtained by adding the following M2 speed control logic, as shown in Fig. 6:

$$T_6 = K_p\left(\dot{\vartheta}_{ref} - \dot{\vartheta}_6\right) + K_i\left(\vartheta_{ref} - \vartheta_6\right) + K_d\left(\ddot{\vartheta}_{ref,F} - \ddot{\vartheta}_{6,F}\right) \tag{6}$$

where K_p, K_i and K_d are the proportional, the integral and the derivative gains, respectively. ϑ_{ref} is the angular position calculated from the vehicle longitudinal dynamics model, as described in Sect. 2.2. Angular accelerations $\ddot{\vartheta}_{ref,F}$ and $\ddot{\vartheta}_{6,F}$ are obtained through a band-limited derivation of $\dot{\vartheta}_{ref}$ and $\dot{\vartheta}_6$, respectively:

$$\begin{cases} t_F \dddot{\vartheta}_{ref,F} + \ddot{\vartheta}_{ref,F} = \ddot{\vartheta}_{ref} \\ t_F \dddot{\vartheta}_{6,F} + \ddot{\vartheta}_{6,F} = \ddot{\vartheta}_6 \end{cases} \tag{7}$$

where t_F is the filter time constant.

Alternative solutions exist in literature for the definition of the PID structure, e.g. the proportional and derivative terms can be placed in the feedback signal rather in the feedback error [16]. Indeed, this alternative structure provides a good disturbance rejection and removes zeros from the closed-loop transfer function thus reducing the overshoot for reference tracking response. To obtain a similar result with the standard PID structure of Eq. (6), a reference prefilter is often used. However, the PID structure selected for the presented activity is constrained by the hardware limitations imposed by the two electric motors drives with a standard control logic as in Eq. (6) with the possibility to tune the three gains and the filtering time constant.

By inserting Eqs. (6) and (7) in (1), the following 8 dynamic equations are obtained:

$$cI_1\ddot{\vartheta}_1 + c_{DMF}\left(\dot{\vartheta}_1 - \dot{\vartheta}_2\right) + c_1\dot{\vartheta}_1 + k_{DMF}\left(\vartheta_1 - \vartheta_2\right) = T_1$$

$$I_2\ddot{\vartheta}_2 + \left(c_2 + \frac{c_{GB1}}{\tau_1^2}\right)\dot{\vartheta}_2 - c_{DMF}\left(\dot{\vartheta}_1 - \dot{\vartheta}_2\right) - \frac{k_{GB1}}{\tau_1}\left(\vartheta_3 - \frac{\vartheta_2}{\tau_1}\right) - k_{DMF}\left(\vartheta_1 - \vartheta_2\right) = 0$$

$$I_3\ddot{\vartheta}_3 + c_3\dot{\vartheta}_3 + c_{SA1}\left(\dot{\vartheta}_3 - \dot{\vartheta}_4\right) + k_{GB1}\left(\vartheta_3 - \frac{\vartheta_2}{\tau_1}\right) + k_{SA1}\left(\vartheta_3 - \vartheta_4\right) = 0$$

$$I_4\ddot{\vartheta}_4 + c_4\dot{\vartheta}_4 + c_{SA1}\left(\dot{\vartheta}_4 - \dot{\vartheta}_3\right) + c_{SA2}\left(\dot{\vartheta}_4 - \dot{\vartheta}_5\right) + k_{SA1}\left(\vartheta_4 - \vartheta_3\right) + k_{SA2}\left(\vartheta_4 - \vartheta_5\right) = 0$$

$$I_5\ddot{\vartheta}_5 + c_5\dot{\vartheta}_5 + c_{SA2}\left(\dot{\vartheta}_5 - \dot{\vartheta}_4\right) + k_{GB2}\left(\vartheta_5 - \frac{\vartheta_6}{\tau_2}\right) + k_{SA2}\left(\vartheta_5 - \vartheta_4\right) = 0$$

$$I_6\ddot{\vartheta}_6 + \left(c_6 + \frac{c_{GB2}}{\tau_2^2} + K_p\right)\dot{\vartheta}_6 - \frac{k_{GB2}}{\tau_2}\vartheta_5 + \left(\frac{k_{GB2}}{\tau_2^2} + K_i\right)\vartheta_6 + K_d\ddot{\vartheta}_{6,F} - K_d\ddot{\vartheta}_{ref,F} = K_p\dot{\vartheta}_{ref} + K_i\vartheta_{ref}$$

$$
I_6 t_F \ddot{\vartheta}_{6,F} + \left(c_6 + \frac{c_{GB2}}{\tau_2^2} + K_P\right)\dot{\vartheta}_6 - \frac{k_{GB2}}{\tau_2}\vartheta_5 + \left(\frac{k_{GB2}}{\tau_2^2} + K_i\right)\vartheta_6 + (I_6 + K_d)\ddot{\vartheta}_{6,F} - K_d\ddot{\vartheta}_{ref,F} = K_P\dot{\vartheta}_{ref} + K_i\vartheta_{ref}
$$

$$
t_F \ddot{\vartheta}_{ref,F} + \ddot{\vartheta}_{ref,F} = \ddot{\vartheta}_{ref} \tag{8}
$$

The introduction of the two additional differential equations in Eq. (7) increases the state vector dimension of the closed-loop system by including the two additional states $\ddot{\vartheta}_{6,F}$ and $\ddot{\vartheta}_{ref,F}$. The tuning of proportional, integral and derivative gains modifies the equivalent damping, stiffness and inertial characteristics of the 6-DOF model. The state-space representation of the closed-loop system is then given by:

$$
\dot{\boldsymbol{x}}_{\boldsymbol{a}} = \boldsymbol{A}_{\boldsymbol{CL}}\boldsymbol{x}_{\boldsymbol{a}} + \boldsymbol{B}_{\boldsymbol{CL}}\boldsymbol{u}_{\boldsymbol{a}} \tag{9}
$$

where $\boldsymbol{x}_{\boldsymbol{a}} = \left\{\boldsymbol{x}^{\boldsymbol{T}}\ \ddot{\vartheta}_{6,F}\ \ddot{\vartheta}_{ref,F}\right\}^T$ is the augmented state vector and $\boldsymbol{u}_{\boldsymbol{a}} = \left\{T_1\ \vartheta_{ref}\ \dot{\vartheta}_{ref}\ \ddot{\vartheta}_{ref}\right\}^T$ is the augmented input vector. Matrices $\boldsymbol{A}_{\boldsymbol{CL}}$ and $\boldsymbol{B}_{\boldsymbol{CL}}$ of the closed-loop system are defined in the Appendix.

Modal Analysis

The complex modal analysis for the closed-loop system in Eq. (9) was carried out and the results for MT gear influence are shown in Figs. 11 and 12 while the DCT gear effect is reported in Figs. 13 and 14. It is important to remark that all simulation results shown in the rest of this subsection are obtained by setting the PID gains to their optimal value reported in Table three; the tuning procedure that led to those controller parameters will be described in Sect. 4.2.

By comparing the closed-loop results in Fig. 12 with the open-loop analysis in Fig. 8, the presence of the speed controller on the motor M2 introduces an additional vibration mode which is represented by the closed-loop second modal shape

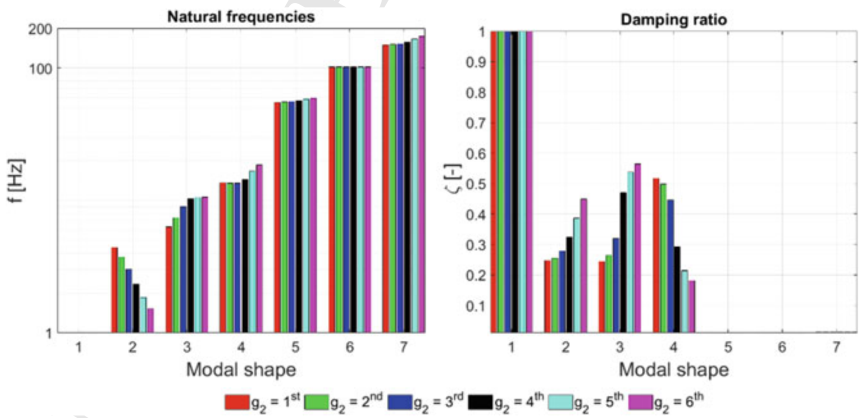

Fig. 11 Natural frequencies and damping ratio of the closed-loop system with different MT gears and DCT gear $g_1 = 5th$

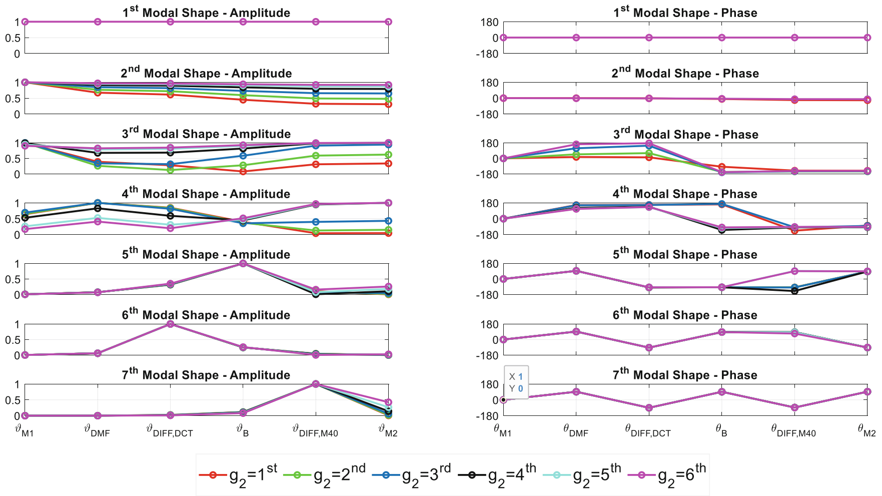

Fig. 12 Modal shape amplitude and phase of the closed-loop system with different MT gears and DCT gear $g_1 = 5th$

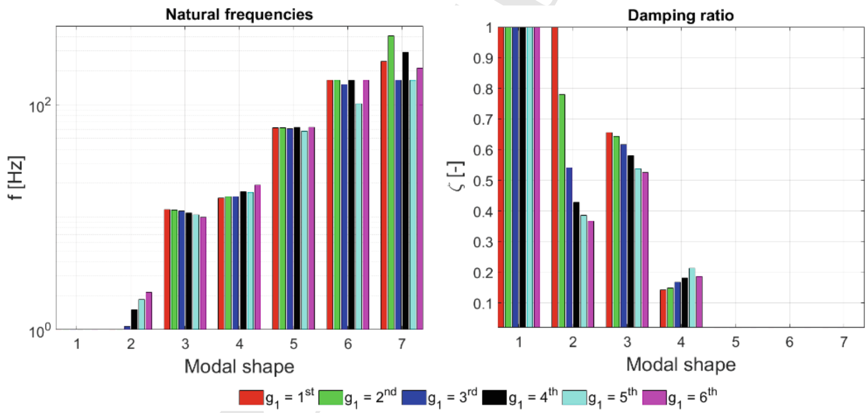

Fig. 13 Natural frequencies and damping ratio of the closed-loop system with different DCT gears and MT gear $g_2 = 5th$

at lower frequencies. The closed-loop modal shapes from the third to the seventh modes corresponds to the open-loop modal shapes from the second to the sixth, respectively. The speed control logic has also a small impact on the natural frequencies while the damping factor of the closed-loop third mode is increased with respect to the correspondent open-loop second mode. It is interesting to note that the speed controller does not influence the modal shape, natural frequency, and damping factor of the last three modes.

509827_1_En_13_Chapter ☑ TYPESET ☐ DISK ☐ LE ☑ CP Disp.:13/1/2022 Pages: 34 Layout: T1-Standard

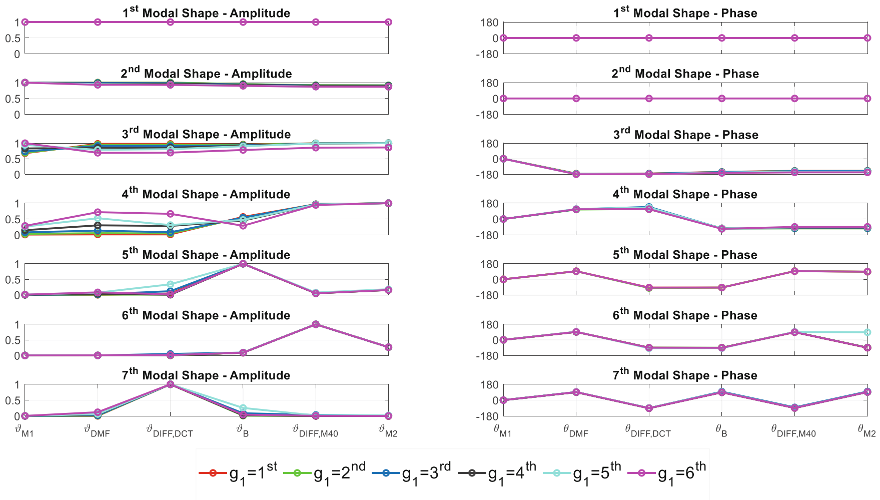

Fig. 14 Modal shape amplitude and phase of the open-loop system with different DCT gears and MT gear $g_2 = 5th$

The effect of the DCT gear g_1 on the open-loop and the closed-loop modal analysis comparison is analyzed in Figs. 13 and 14.

The DCT gear ratio has a lower influence on the modal shape of the additional mode (the second) introduced by the closed-loop system. Even if the closed-loop is still beneficial in increasing the damping factor of the third and fourth modes, respect to the equivalent second and third open-loop modes, the variation of the DCT gear ratio is not as effective as observed for the variation of the MT gear.

3.3 Model Experimental Validation

A torsional vibration test is executed on the DCT test rig to obtain the experimental data and validate the linear model described and analyzed in the previous sections. During the test, one electric motor (e.g. M2) is controlled to apply a sinusoidal torque with a constant amplitude and a continuously variable frequency, while the second motor (M1) is controlled to keep a constant speed. Before the torsional vibration test is started, a preliminary phase is required to bring the transmission test rig into a steady-state condition, identified by constant torque and speed, where the behavior of the system can be linearized through Eq. (1). The preliminary phase is fundamental to keep approximately constant the system parameters, e.g. torsional stiffnesses, and to avoid any inversion of torque sign thus preventing nonlinear phenomena such as the impact between rotating components due to backlash.

Time histories of the torques applied by the two electric motors are measured together with the angular speeds in three points of the transmission line ($\dot{\theta}_1 = \dot{\theta}_{M1}$, $\dot{\theta}_3$, and $\dot{\theta}_6 = \dot{\theta}_{M2}$).

The sinusoidal torque applied by the M2 motor is:

$$T_6 = \overline{T} + T_0 \sin(2\pi f(t)t) \tag{10}$$

where $\overline{T}$ is a mean value of torque constantly applied during the test to create a torsional preload in the transmission system (to avoid nonlinearities), T_0 is the torque amplitude and $f(t)$ the excitation frequency calculated as a power function of the time t (logarithmic chirp):

$$f(t) = f_0 \left(\frac{f_1}{f_0} \right)^{\frac{t}{t_1}} \tag{11}$$

where f_0 is the initial frequency and f_1 is the final frequency at time t_1.

Experimental measurements are then processed resulting in the Frequency–Response Functions (FRFs) between the input torque T_6 applied by M2 and the three rotational speeds. Under the assumption that the system is linear (at least in the neighborhood of the equilibrium point around which the system vibrates) and characterized by time-invariant parameters, the estimation of a FRF from experimental data can be performed by calculating the Power Spectral Density (PSD) and the Cross-Power Spectral Density (CSD) through the Welch's method [17].

Figures 15 and 16 show the estimated FRFs from the measurements together with their coherence functions to evaluate the frequency range for which the estimation algorithm is considered reliable.

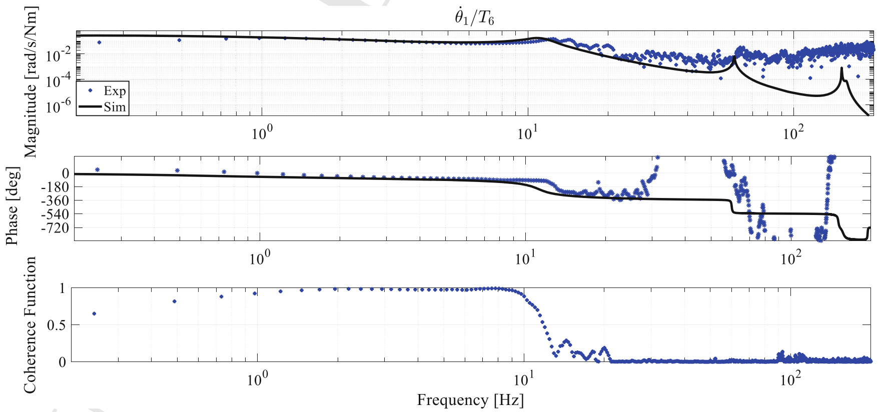

Fig. 15 FRF $\dot{\theta}_1/T_6$ resulting from the experimental measurements and calculated using the open-loop linear model with $g_1 = 3rd$ and $g_2 = 4th$

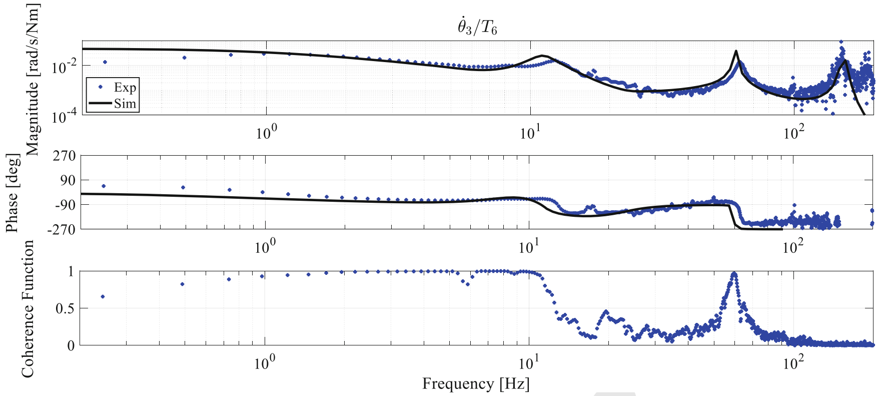

Fig. 16 FRF $\dot{\theta}_3/T_6$ estimated from the experimental measurements and calculated from the open-loop linear model with $g_1 = 3rd$ and $g_2 = 4th$

Since the excitation for the dynamic system is generated by the electric motor M2, the amplitude of the $\dot{\theta}_3/T_6$ and $\dot{\theta}_6/T_6$ responses are high enough to be measured accurately by the encoder up to more than 150 Hz. On the other hand, the lower amplitude of oscillation for the other M1 motor limits the range of reliability of $\dot{\theta}_1/T_6$ to 20 Hz.

The results concerning the first FRF ($\dot{\theta}_1/T_6$) are affected by a relevant phase difference in the high frequency range, and this is mainly due to very low signal to noise ratio in the experimental measures rather than to the model, as also confirmed by the coherence function that drops to zero very quickly after 20 Hz.

On the other hand, the experimental FRF of $\dot{\theta}_3/T_6$ is very well estimated from the encoder measurements in the whole frequency range, thanks to the high peak amplitudes and the high encoder resolution. Furthermore, the linear model can capture both the experimental magnitude and phase up to more than 200 Hz.

Finally, the FRF of $\dot{\theta}_6/T_6$ is shown in Fig. 17, where the accuracy of the experimental estimation decreases significantly immediately after the third peak in magnitude. However, the FRF magnitude and phase is also well captured by the linear model within the validation range of the experimental estimation.

4 Sensitivity Analysis of the Linear Model

The experimentally validated DCT torsional model represents an important tool for predicting and calibrating the effect of the two motor controllers on the test rig dynamic behavior. The present section aims at analyzing the DCT model sensitivity to the parameters that are subject to calibration, e.g. the speed control logic gains, or to optimization for accomplishing the desired operative condition, e.g. the DCT or MT gear ratio.

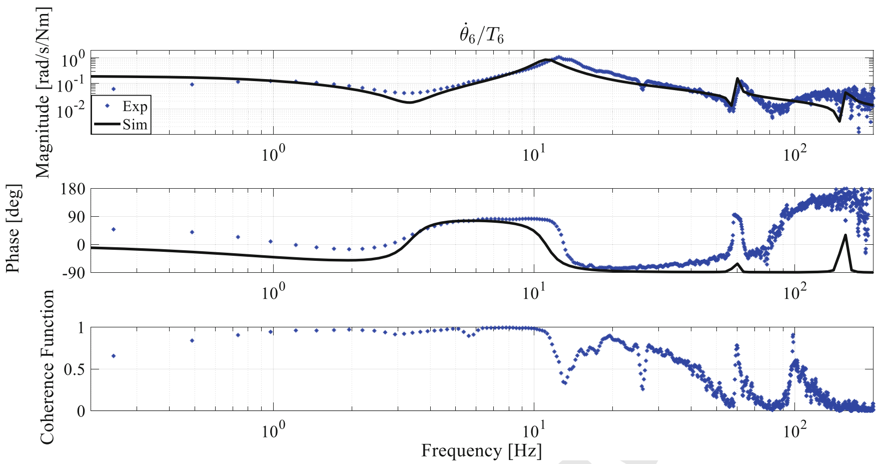

Fig. 17 FRF $\dot{\theta}_6/T_6$ estimated from the experimental measurements and calculated from the open-loop linear model with $g_1 = 3rd$ and $g_2 = 4th$

The sensitivity analysis is carried out in the frequency domain by considering the frequency response functions between the closed-loop system input (M1 motor torque T_1 and reference speed $\dot{\theta}_{ref}$) and the desired output quantities selected for evaluating the DCT test rig performance. One of the main tasks for the considered HiL test rig is to regulate the brake disk speed $\dot{\theta}_4$ to track the reference angular speed calculated from the vehicle model. However, the speed control logic in Eq. (6) is applied to the M2 motor speed $\dot{\theta}_6$. Based on these considerations, four FRFs are evaluated from the closed-loop system described by the state space in Eq. (9): two Reference Speed Tracking (RST) FRFs for evaluating the controller tracking performance and two Disturbance Rejection (DR) FRFs for analyzing the M2 controller sensitivity to the application of the M1 motor torque.

The two RST FRFs are obtained by considering a harmonic excitation for the reference speed $\dot{\theta}_{ref}$ with amplitude $\dot{\theta}_{ref,0}$ and frequency Ω by fixing the M1 torque $T_1 = 0$:

$$\boldsymbol{\alpha}_{\mathbf{RST}}(\Omega) = \left[G^4_{RST}(\Omega)\ G^6_{RST}(\Omega) \right]^T = \boldsymbol{C}(j\Omega \boldsymbol{I} - \boldsymbol{A}_{CL})^{-1}\boldsymbol{B}_{CL}\left[0\ 1/(j\Omega)\ 1\ j\Omega\right]^T \tag{12}$$

where $\boldsymbol{C} = \left[0\,0\,0\,0\,0\,0\,0\,0\,0\,1\,0\,1\,0\,0\right]^T$ is the output matrix; $G^4_{RST} = \tau_2\dot{\theta}_{4,0}/\dot{\theta}_{ref,0}$ and $G^6_{RST} = \dot{\theta}_{6,0}/\dot{\theta}_{ref,0}$ are the RST FRFs from the reference speed to the disk brake $\dot{\theta}_4$ and to the M2 motor speed $\dot{\theta}_6$, respectively.

The desired shape for both the RST FRFs is $G^4_{RST}(\Omega) = G^6_{RST}(\Omega) = 1$ for $\Omega < \Omega_B$ where Ω_B represents the closed-loop bandwidth frequency above which it is required to drop for reducing the sensitivity to high frequency noises.

The two DR FRFs are computed by considering a harmonic excitation for the M1 torque T_1 with amplitude $T_{1,0}$ and frequency Ω by fixing the reference speed $\theta_{ref} = \dot{\theta}_{ref} = \ddot{\theta}_{ref} = 0$:

$$\boldsymbol{\alpha}_{\mathbf{DR}}(\Omega) = \left[\, G^4_{DR}(\Omega)\ G^6_{DR}(\Omega) \,\right]^T = \boldsymbol{C}(j\Omega \boldsymbol{I} - \boldsymbol{A}_{CL})^{-1} \boldsymbol{B}_{CL} \left[\, 1\ 0\ 0\ 0 \,\right]^T \qquad (13)$$

where $G^4_{DR} = \dot{\theta}_{4,0}/T_{1,0}$ and $G^6_{DR} = \dot{\theta}_{6,0}/T_{1,0}$ are the DR FRFs from the M1 torque T_1 to the disk brake $\dot{\theta}_4$ and to the M2 motor speed $\dot{\theta}_6$, respectively.

The desired shape for both the DR FRFs is $G^4_{DR}(\Omega) = G^6_{DR}(\Omega) = 0$ for the whole frequency range.

4.1 *Sensitivity to Gear Ratios*

The first analysis concerns the model sensitivity to the variation of the DCT gear ratio, which is a parameter imposed by the TCU having a strong influence on the test bench dynamics and the motor controller performance. The PID gains of the speed controller are set to the nominal values reported in Table three.

Figure 18 shows the trend of the RST and DR FRFs when the DCT gear ratio is changed, and the MT gear ratio is kept constant to $g_2 = 5th$.

Both RST FRFs show a clear resonance peak at the first natural frequency that increases with the DCT gear ratio, as already shown in Fig. 13. The amplitude of the first resonance peak increases with the DCT gear ratio thus reflecting the

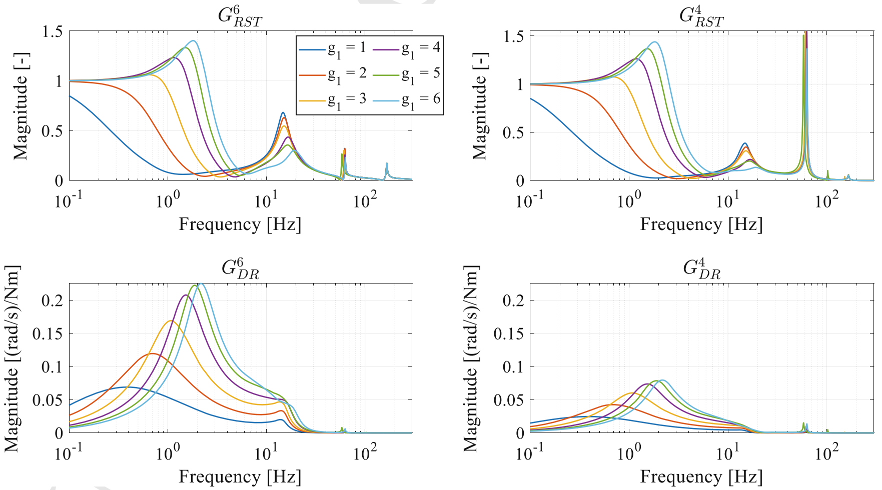

Fig. 18 DR and RST FRFs magnitude for the closed-loop system with different DCT gears and MT gear $g_2 = 5th$

509827_1_En_13_Chapter ☑ TYPESET ☐ DISK ☐ LE ☑ CP Disp.:13/1/2022 Pages: 34 Layout: T1-Standard

damping ratio characteristics obtained from the modal analysis in Fig. 13. A second resonance peak is also visible for the G^6_{RST} FRF whose frequency increases with the DCT gear but its amplitude decreases for higher gears. A similar shift of the resonance frequencies is obtained for the G^4_{RST} FRF but the amplitude of the second and the third peaks are more pronounced than their correspondents in G^6_{RST}. This result agrees with the modal shape of the fifth mode (~60 Hz) in Fig. 14 where the brake disk inertia vibrates with respect to the remaining part of the driveline, which stays practically stationary.

The effect of the motor M1 torque is analyzed through the two DR FRFs plotted in Fig. 18. The influence of the M1 torque on $\dot{\theta}_6$ and $\dot{\theta}_4$ dynamics is more pronounced for G^6_{DR} than G^4_{DR} and amplifies the first peak for higher DCT gears.

The main conclusion for the sensitivity analysis on the DCT gear variation is that the dynamic behavior of the M2 speed controller is improved in terms of disturbance rejection from M1 when the first gear is engaged in the DCT. However, the reference tracking attitude for $g_1 = 1$ does not represent the best selection since the closed-loop bandwidth is drastically reduced if compared to higher gears RST FRFs.

The second sensitivity analysis involves the variation of the MT gear ratio, considered as a tunable parameter for extending the test rig operative speed and torque range based on the maneuver selection. The effect of τ_2 on the RST FRFs is shown in Fig. 19 by engaging the fifth DCT gear.

The effect of MT gear on the first peak of both G^6_{RST} and G^6_{RST} is opposite if compared to the DCT sensitivity analysis in Fig. 18: the resonance frequency and the peak amplitude decreases with MT gear. Moreover, the first and second peaks tends to get closer for lower gears so that they produce a single peak for G^6_{RST} when $g_2 = 1$. The sixth gear would represent a good choice in terms of reference tracking

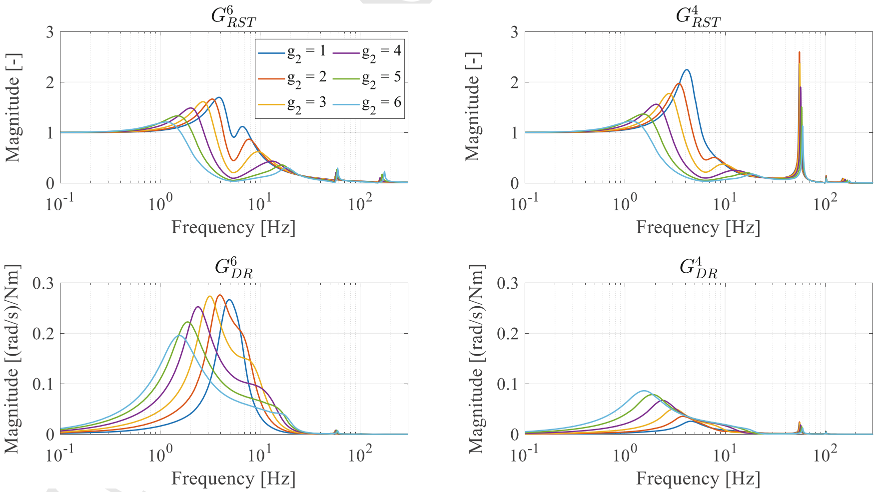

Fig. 19 RST and DR FRFs magnitude for the closed-loop system with different MT gears and DCT gear $g_1 = 5th$

performance due to the lower amplitude of the first peak, even if this advantage is obtained with a lower closed-loop bandwidth, if compared to other gears. Finally, the DR FRFs modification to the MT gear ratio variation is reported in Fig. 19. The influence of M1 torque on the M2 speed controller dynamics is still more predominant on G^6_{DR} than G^4_{DR}. The selection of higher gears reduces the first peak amplitude for G^6_{DR} while a lower gear is beneficial for attenuating G^4_{DR}.

The sensitivity analysis on the MT gear ratio variation led to the conclusion that the sixth gear represents an optimal solution to always guarantee the desired reference tracking performance and external disturbance rejection. However, the actual usage of the HiL test bench requires to run the desired maneuver considering also the constraints imposed by the power and torque limitations of the two electric motors, that may require a different gear selection from the optimal solution. Therefore, the performance of the test bench must be carefully verified with all the possible combinations of gear ratios.

4.2 Sensitivity to PID Gains

Differently from the mechanical parameters such as the DCT and MT gear ratios, the PID gains as well as the filter time constant t_F, can be tuned and eventually adapted to the test rig operative conditions with more flexibility.

The effect of the speed proportional gain K_p on the RST FRFs is evaluated in Fig. 20 where the fifth gear is set for both DCT and MT.

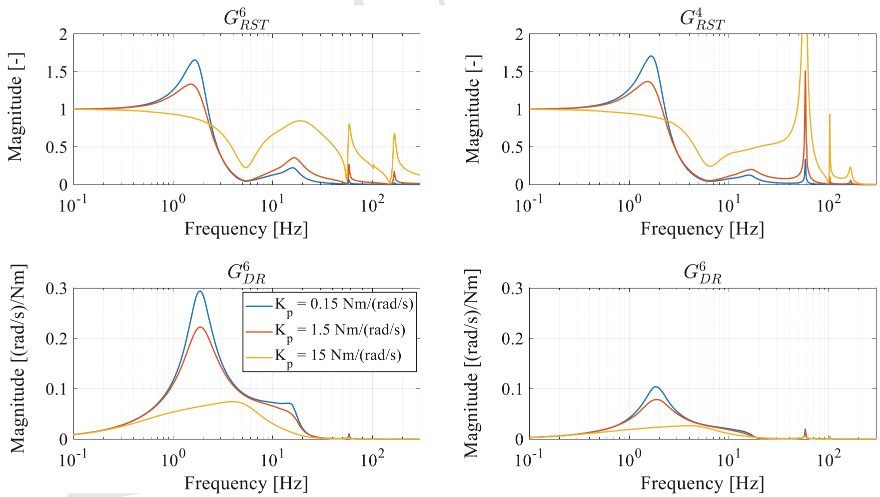

Fig. 20 RST and DR FRFs magnitude for the closed-loop system with different proportional gains K_p, by setting $K_i = 75$ Nm/rad, $K_d = 0.75$ Nm/(rad/s^2), $t_F = 100$ s, $g_1 = 5th$ and $g_2 = 5th$

The proportional speed gain cannot shift none of the resonance frequencies referring to both G^6_{RST} and G^4_{RST} but it can modify their amplitude values. The reason behind that is well explained by Eq. (8) where K_p modifies the multiplicative coefficient of $\dot{\theta}_6$. An increment of K_p would improve the reference tracking performance by reducing the first peak amplitude and by extending the closed-loop bandwidth. However, the benefits achieved with a high K_p gain on the G^6_{RST} FRF produces a negative effect on the G^4_{RST} FRF for the high frequency range. This aspect aims at remarking that even a fine tuning of the M2 speed controller may provoke excessive oscillations in other driveline parts and then transmitted to the test rig supports in terms of vibrations or noises perceived by the user. A similar sensitivity analysis for the disturbance rejection FRFs is shown in Fig. 20 where an increment of K_p is positive for both G^6_{DR} and G^4_{DR} in terms of resonance peak attenuation.

The effect of the integral gain K_i on the RST and DR FRFs is then evaluated in Fig. 21.

Differently from the proportional gain, the integral contribution can shift the resonance frequency of the first peak since it modifies the stiffness contribution in Eq. (8) for the last degree of freedom (motor M2). The main benefit of increasing the integral gain is the extension of the closed-loop bandwidth but at the cost of a more pronounced peaks amplitude in the whole frequency range. An increment of K_i also produces a shift of the DR FRFs first resonance peak towards higher frequencies and it shrunk the frequency band around the peak, as visible for both G^6_{DR} and G^4_{DR}. Another benefit from the increment of the integral contribution is the attenuation of the G^6_{DR} peak amplitude meanwhile G^4_{DR} amplitude is not influenced by the variation of this parameter.

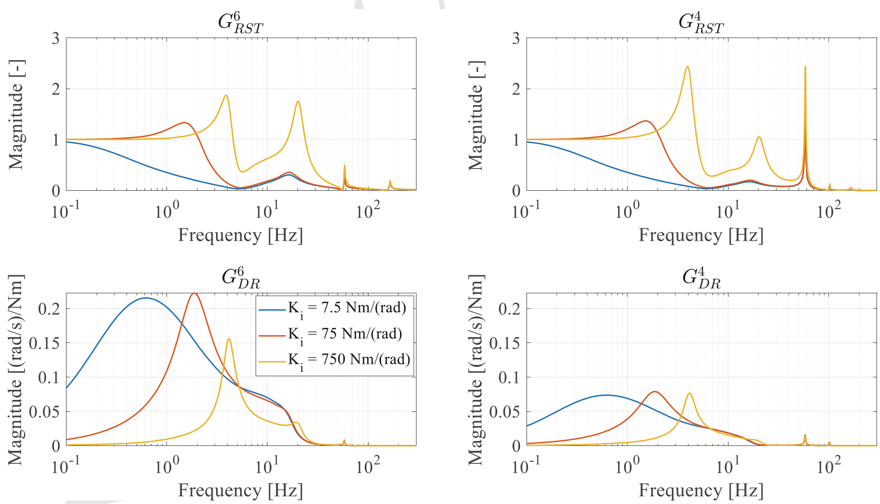

Fig. 21 RST FRFs magnitude for the closed-loop system with different integral gains K_i, by setting $K_p = 1.5$ Nm/(rad/s), $K_d = 0.75$ Nm/(rad/s^2), $t_F = 100$ s, $g_1 = 5th$ and $g_2 = 5th$

509827_1_En_13_Chapter ✓ TYPESET DISK LE ✓ CP Disp.:13/1/2022 Pages: 34 Layout: T1-Standard

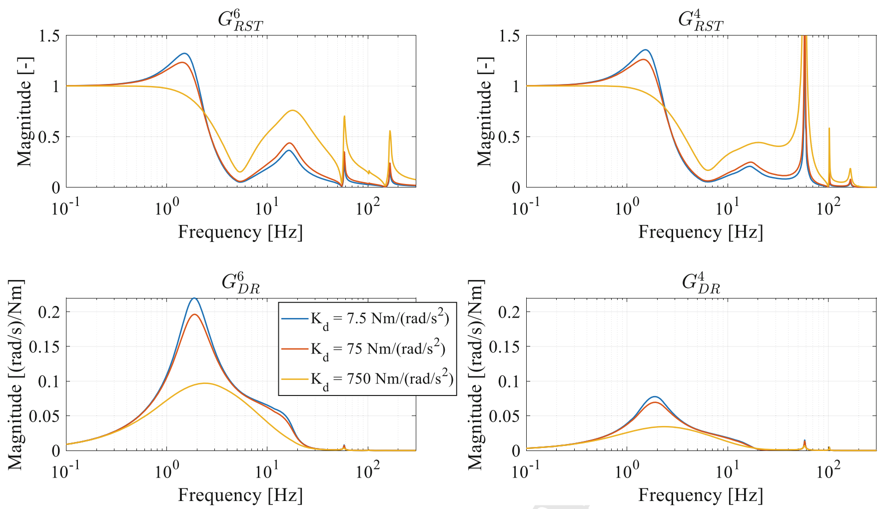

Fig. 22 RST and DR FRFs magnitude for the closed-loop system with different derivative gains K_d, by setting $K_p = 1.5$ Nm/(rad/s), $K_i = 75$ Nm/rad, $t_F = 100$ s, $g_1 = 5th$ and $g_2 = 5th$

Furthermore, the effect of the derivative PID gain on both RST and DR FRFs is shown in Fig. 22.

The derivative gain can modify the peaks amplitude, but it cannot shift any resonance frequency. The positive benefit of a high derivative gain is the reduction of the first peak magnitude for both G^6_{RST} and G^4_{RST} but at the cost of an increment in the peak amplitudes for higher frequencies, especially for G^4_{RST}. A similar conclusion is observed for the DR FRFs, where an increment of K_d is beneficial for the whole frequency range in terms of peak attenuation but at the cost of a larger frequency band pass.

Finally, the impact of the filter time constant t_F on both RST and DR FRFs is illustrated in Fig. 23. It can be seen that, the effect of the filter time constant on system dynamics in the low-mid frequency range is non monotonic: for low values of t_F, an additional damping to the first resonant mode is obtained; on the contrary, for high values, a further increase reduces the damping and increases the frequency of the main peaks of all the considered FRFs. On the other hand, at high frequencies, the effect of the time constant increment is always to attenuate the response of both RST. This last effect is particularly beneficial in this application, where high frequency disturbances are generated by the staircase encoder speed signals that requires to filter out this high frequency content to avoid NVH issues during the test.

The results obtained through the sensitivity analysis of the M2 speed controller parameters, represent a valid tool for calibrating the PID gains thus achieving a closed-loop FRF response which can be shaped according to the desired requirements reported in Table 2. The desired shape for both G^6_{RST} and G^4_{RST} FRFs magnitudes should be constrained as close as possible to 1 to satisfy the reference tracking performance. However, this can be achieved only within the frequency bandwidth

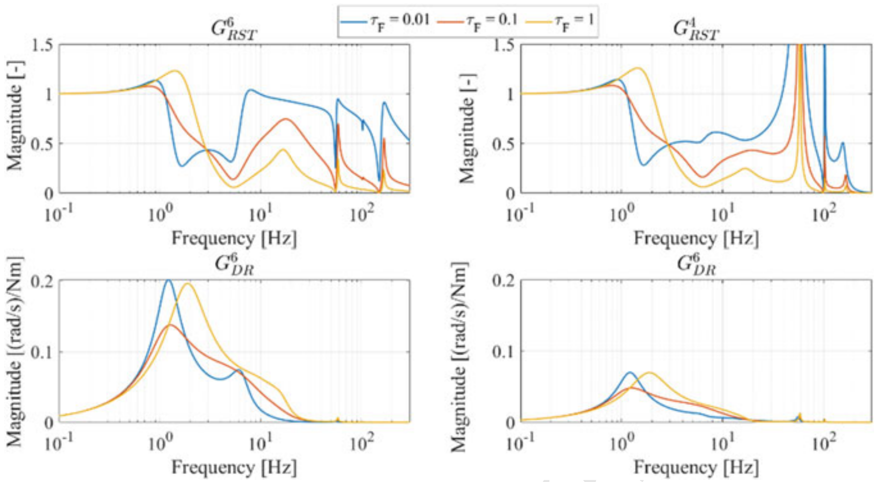

Fig. 23 RST and DR FRFs magnitude for the closed-loop system with different filter time constant t_F, by setting $K_p = 1.5$ Nm/(rad/s), $K_i = 75$ Nm/rad, $K_d = 0.75$ Nm/(rad/s^2), $g_1 = 5th$ and $g_2 = 5th$

Table 2 Desired FRF requirements for PID calibration

Property	Requirements
Peak amplitude of G^6_{RST}	≤ 1.3
Peak amplitude of G^4_{RST}	≤ 1.5
Bandwidth of G^6_{RST} (at half-power point)	≥ 2 Hz
Bandwidth of G^6_{DR} (at half-power points)	≤ 4 Hz
Peak amplitude of G^6_{DR}	≤ 0.25(rad/s)/Nm

range, that is the frequency range where the magnitude of a closed-loop FRF is greater than − 3 dB. The sensitivity analysis shows that the most effective parameter to extend the frequency bandwidth is the integral contribution K_i. An excessive selection of the integral gain produces an increment of all resonance peak amplitudes, thus reducing the reference tracking performance. This negative consequence can be in part compensated by increasing the proportional and the derivative gains to smooth the peaks, at least in the lower frequency range. The amplitude of the G^4_{RST} peaks also require a constraint to avoid an undesired vibration level in any other point of the driveline. Indeed, since the closed-loop system is feedbacked on the M2 motor speed, the magnitude constraint for G^4_{RST} peaks is set higher than G^6_{RST} FRF.

To keep the desired reference tracking performance achieved for RST FRSs, the influence of the M1 motor torque should be also mitigated by shaping G^6_{DR} and G^4_{DR}. The sensitivity analysis proved that G^6_{DR} represents the more critical FRF in terms of resonance peaks amplitude and on the peak frequency band which can be shrunk

Table 3 Final values of PID gains

Gain	Value
Proportional gain K_p	1.5 Nm/(rad/s)
Integral gain K_i	75 Nm/(rad)
Derivative gain K_d	0.75 Nm/(rad/s^2)
Derivative time constant t_F	100 s

with an increment of the integral gain and a reduction of proportional and derivatives gains.

To achieve the required dynamic performance of the closed-loop system reported in Table 3, a brute force method is applied to search for a suitable set of PID gains among a predefined range of values. The lower and the upper limits of each PID parameter range are defined based on the sensitivity analysis carried out in the present section, thus constraining the brute force algorithm to test only the set of gains that provoke an perceptible variation of the RST and DR frequency responses. The final gains computed by the brute force algorithm are then reported in Table 3:

The final set of PID parameters clearly shows that the solution computed by the brute force algorithm provides a low derivative gain with a high filtering time constant, whose combined effect produces a negligible intervention of the derivative term. Indeed, Fig. 22 clearly demonstrates that only a derivative gain of two magnitude order greater than the nominal value would modify the frequency response of the closed-loop system. The calibrated speed controller is then verified through the time domain response of the closed-loop system, by providing a delayed step input between $\dot{\theta}_{ref}$ and T_1. Time histories results of $\dot{\theta}_6$, $\dot{\theta}_4$ and T_6 are shown in Fig. 24.

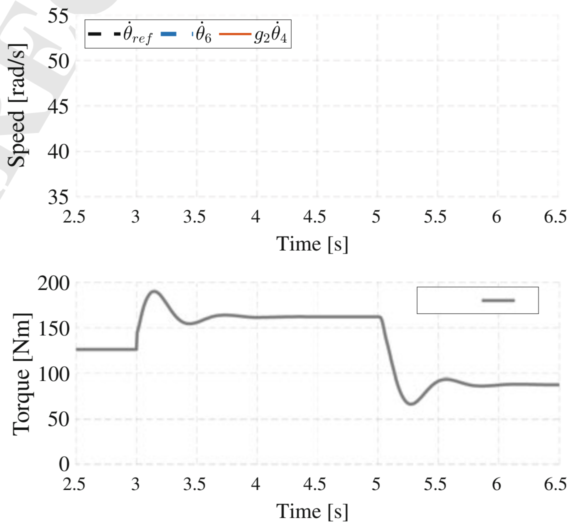

Fig. 24 Time response of $\dot{\theta}_6$ and $\dot{\theta}_4$ to a delayed step input between $\dot{\theta}_{ref}$ and T_1 with $g_1 = 5th$ and $g_2 = 5th$

The speed controller on M2 provides satisfactory response in terms of reference speed tracking performance with an overshoot of 5.6%, a rise time of 0.2 s and a settling time of 0.4 s. The step torque on T_1, applied 2 s later after the imposition of the step on the reference speed, provides useful information regarding the capability of the controller to react to external disturbance. Even if the M1 torque T_1 produces a 16% overshoot on $\dot{\theta}_6$ and $\dot{\theta}_4$, the closed-loop system can reject the torque disturbance after 1 s.

5 Controller Experimental Validation

The PID gains selected through the sensitivity analysis described in the previous section, are then implemented to the transmission test rig for validating the controller performance. The controller performance is validated both in frequency and time domain to prove its efficiency in terms reference tracking accuracy and disturbance rejection to external torques. To guarantee that the transmission works as much as possible in a linear operating range, before the execution of any experiments, the test rig is brought into a steady-state condition identified by a constant angular speed, imposed by the speed controller of M2, and by a transmission torsional preload through the application of a constant torque from the motor M1. This procedure is necessary to avoid the inversion of the torque sign which is responsible for extremely non-linear gear teeth impact due to the torsional backlashes between transmission rotating components [11, 18].

During the first test, the M2 electric motor is controlled in speed through the PID logic in Eq. (6) and parametrized according to Table 3. A sinusoidal speed with a constant amplitude and a continuously variable frequency is generated for $\dot{\theta}_{6,ref}$:

$$\dot{\theta}_{ref} = \dot{\theta}_m + \dot{\theta}_a \sin(2\pi f(t)t) \tag{14}$$

where $\dot{\theta}_m$ and $\dot{\theta}_a$ are the mean and the amplitude values of the sinusoidal signal, respectively. $f(t)$ is calculated to obtain a logarithmic chirp as described in Eq. (11). The second motor (M1) is controlled to apply a constant torque T_1 to guarantee the desired preload. The measured M2 motor speed is than elaborated, together with $\dot{\theta}_{ref}$, to estimate the experimental RST FRF, according to the algorithm described in Sect. 3.3. The experimental estimation of G^6_{RST} is then compared to the linear model RST FRF in Fig. 25.

The experimental G^6_{RST} is well estimated up to 40 Hz, above which the coherence function drops to zero. The good match between the experimental FRF with the linear model response proves that the PID gains tuned through the sensitivity analysis described in Sect. 4, can guarantee the desired RST performance also for the transmission test rig.

The M2 speed controller is furtherly investigated through a second experiment that aims at validating its robustness against the application of a dynamic external torque

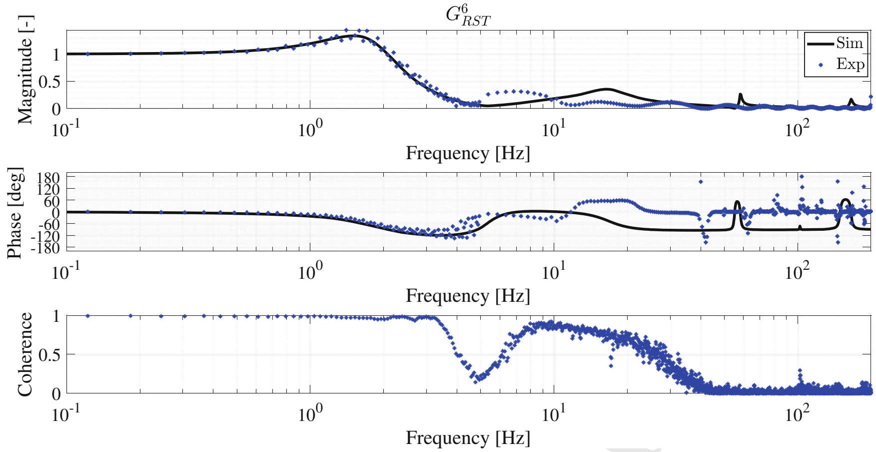

Fig. 25 Experimental estimation and model evaluation of G^6_{RST} by fixing $K_p = 1.5$ Nm/(rad/s), $K_i = 75$ Nm/rad, $K_d = 0.75$ Nm/(rad/s^2), $t_F = 100$ s $g_1 = 5th$ and $g_2 = 5th$

from the electric motor M1. The M2 motor is controlled to keep a constant speed meanwhile a sinusoidal torque signal with a constant amplitude and a continuously variable frequency is applied by M1:

$$T_1 = T_{1,m} + T_{1,a} \sin(2\pi f(t)t) \tag{15}$$

where $T_{1,m}$ and $T_{1,a}$ are the mean and the amplitude values of the sinusoidal signal, respectively. $f(t)$ is calculated to obtain a logarithmic chirp as described in Eq. (11). The M1 torque is measured, as well as the M2 speed $\dot{\theta}_6$, to elaborate the estimation of G^6_{DR} which is compared against the linear model DR FRF in Fig. 26.

Within the frequency validation range of the experimental G^6_{DR} (up to 40 Hz), the M2 speed controller shows disturbance rejection properties even better than the desired requirements imposed in Table 2 as proved by the lower peak amplitude around 2 Hz.

Finally, the speed controller is verified in the time domain by imposing a step signal to the reference signal $\dot{\theta}_{ref}$. The experimental time histories of the M2 motor speed is compared against the linear transmission model step response in Fig. 27.

The experimental M2 motor speed is characterized by a quick response during the initial phase of the step application, mainly due to the presence of the second resonance peak at ~ 20 Hz visible in Fig. 25, followed by a slower dynamics dictated by the first resonance peak at ~ 2 Hz. The mismatch observed between the experimental and simulation results in Fig. 27 is larger than what expected from the frequency-domain comparison. This discrepancy is mainly due to the intervention of the nonlinear transmission behavior during the test execution. The main nonlinearities in an automotive transmission system are backlashes and angular clearances between the rotating components (meshing gears and synchronizers). Indeed, the

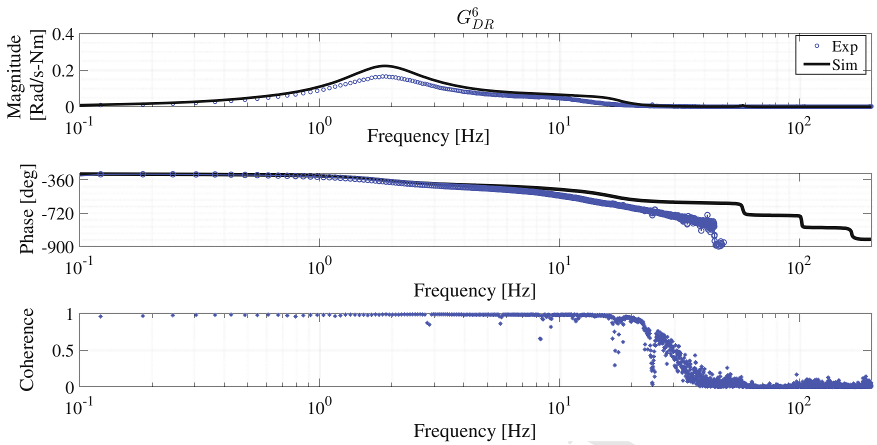

Fig. 26 Experimental estimation and model evaluation of G^6_{DR} by fixing $K_p = 1.5$ Nm/(rad/s), $K_i = 75$ Nm/rad, $K_d = 0.75$ Nm/(rad/s^2), $t_F = 100$ s $g_1 = 5th$ and $g_2 = 5th$

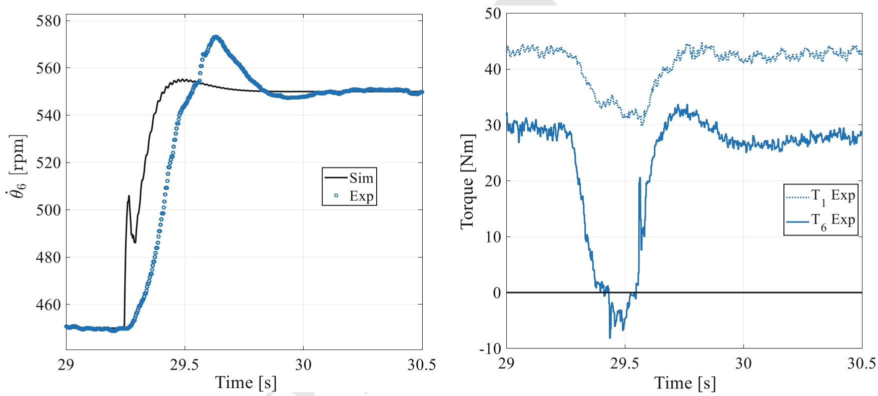

Fig. 27 Experimental and analytical time response of $\dot{\theta}_6$, T_1 and T_6 by fixing $K_p = 7.5$ Nm/(rad/s), $K_i = 75$ Nm/rad, $K_d = 0.75$ Nm/(rad/s^2), $t_F = 100$ s, $g_1 = 5th$ and $g_2 = 5th$

second subplot of Fig. 27 shows a typical nonlinear trend of the torque entering the MT gearbox. A torque sign inversion characterized by a dead band is clearly visible; it is related to a loss of contact between internal rotating components of MT gearbox due to load reversal. The loss of contact after zero crossing is followed by torsional impacts which generate peaks in the instantaneous torque trend (see also [11, 19] for further details). The effect of backlash nonlinearities is to make the MT working in an operating condition far from the linear hypothesis assumed for system modelling. Nevertheless, the performance of the controlled system in time domain is still satisfactory even if the system dynamic behavior is quite different from the one used for controller parameter tuning. On the other hand, the sine-sweep test used for elaborating the experimental FRFs in Fig. 26, is executed with a constantly applied mean torque $T_{1,m}$ (see Eq. 10) that guarantees a minimum level of torsional preload that avoid any backlashes recovery. A similar conclusion is also valid for the sine-sweep results of Fig. 25, where the combination of a low sine amplitude $\dot{\theta}_a$ with a constant preload T_1 constrains the transmission test rig to work in a linear operating condition thus justifying a better match with the simulated FRF.

6 Conclusions

This paper provided a model-based tuning procedure for controlling the electric motors of a transmission HiL test rig with the aim of achieving the desired closed-loop requirements with the following main conclusions.

- HiL transmission test rigs require an accurate calibration of the torque and speed feedback controllers of the actuators, e.g. electric motors, used to emulate the external load applied to the system under investigation, e.g. a DCT.
- The dynamic behavior of the driveline mounted on the test bench is well described by the proposed linear 6-DOF transmission model, for both open-loop and closed-loop configurations, as long as the transmission test rig operates in linear conditions, e.g. avoiding torque sign inversion.
- The step change of the gear ratio of the transmission under test during normal operation of the bench has a relevant effect on system torsional dynamics. Potential future developments could involve an adaptation of the control parameters to achieve satisfactory performance in all the operating conditions. However, most of industrial drives typically do not allow a gain scheduling of the motor controllers during the test execution.
- A novel methodology for analyzing and tuning the reference speed tracking and disturbance rejection performance of the motor controllers, both in frequency and time domains has been explained. The sensitivity analysis helps to understand the effect of each mechanical and control parameter on the system dynamics thus guiding the calibration process.
- The application of this method to the DCT HiL test rig installed at Politecnico di Torino provided a good tradeoff between the conflicting requirements (reference speed tracking and disturbance rejection). The torsional vibration analysis of the system revealed the presence of an underdamped mode that could be excited by high frequencies noises related to speed or torque feedback signals. This requires a speed controller design that must include the analysis of the internal dynamics of the whole transmission and driveline to avoid NVH issues during normal operation of the bench.

509827_1_En_13_Chapter ☑ TYPESET ☐ DISK ☐ LE ☑ CP Disp.:13/1/2022 Pages: 34 Layout: T1-Standard

Appendix—Closed-Loop State Space Matrices

$$\boldsymbol{A}_{CL} = \begin{bmatrix} \boldsymbol{A}_{11} & \boldsymbol{A}_{12} & \boldsymbol{A}_{13} \\ \boldsymbol{A}_{21} & \boldsymbol{A}_{22} & \boldsymbol{A}_{23} \end{bmatrix}$$

where:

$$\boldsymbol{A}_{11} = \boldsymbol{O}_{6X6};\ \boldsymbol{A}_{12} = \boldsymbol{I}_{6X6};\ \boldsymbol{A}_{13} = \boldsymbol{O}_{6X2}$$

$$\boldsymbol{A}_{21} = \begin{bmatrix} -\frac{k_{DMF}}{I_1} & \frac{k_{DMF}}{I_1} & 0 & 0 & 0 & 0 \\ \frac{k_{DMF}}{I_2} & -\frac{\left(k_{DMF}+\frac{k_{GB1}}{\tau_1^2}\right)}{I_2} & \frac{k_{GB1}}{\tau_1 I_2} & 0 & 0 & 0 \\ 0 & \frac{k_{GB1}}{\tau_1 I_3} & -\frac{(k_{GB1}+k_{SA1})}{I_3} & \frac{k_{SA1}}{I_3} & 0 & 0 \\ 0 & 0 & \frac{k_{SA1}}{I_4} & -\frac{(k_{SA1}+k_{SA2})}{I_4} & \frac{k_{SA2}}{I_4} & 0 \\ 0 & 0 & 0 & \frac{k_{SA2}}{I_5} & -\frac{(k_{SA2}+k_{GB2})}{I_5} & \frac{k_{GB2}}{\tau_2 I_5} \\ 0 & 0 & 0 & 0 & \frac{k_{GB2}}{\tau_2 I_6} & -\frac{\left(\frac{k_{GB2}}{\tau_2^2}+K_i\right)}{I_6} \\ 0 & 0 & 0 & 0 & \frac{k_{GB2}}{\tau_F \tau_2 I_6} & -\frac{\left(\frac{k_{GB2}}{\tau_2^2}+K_i\right)}{\tau_F I_6} \\ 0 & 0 & 0 & 0 & 0 & 0 \end{bmatrix}$$

$$\boldsymbol{A}_{22} = \begin{bmatrix} -\frac{(c_{DMF}+c_1)}{I_1} & \frac{c_{DMF}}{I_1} & 0 & 0 & 0 & 0 \\ \frac{c_{DMF}}{I_2} & -\frac{\left(c_{DMF}+c_2+\frac{c_{GB1}}{\tau_1^2}\right)}{I_2} & 0 & 0 & 0 & 0 \\ 0 & 0 & -\frac{(c_3+c_{SA1})}{I_3} & \frac{c_{SA1}}{I_3} & 0 & 0 \\ 0 & 0 & \frac{c_{SA1}}{I_4} & -\frac{(c_{SA1}+c_4+c_{SA2})}{I_4} & \frac{c_{SA2}}{I_4} & 0 \\ 0 & 0 & 0 & \frac{c_{SA2}}{I_5} & -\frac{(c_5+c_{SA2})}{I_5} & 0 \\ 0 & 0 & 0 & 0 & 0 & -\frac{\left(c_6+\frac{c_{GB2}}{\tau_2^2}+K_p\right)}{I_6} \\ 0 & 0 & 0 & 0 & 0 & -\frac{\left(c_6+\frac{c_{GB2}}{\tau_2^2}+K_p\right)}{\tau_F I_6} \\ 0 & 0 & 0 & 0 & 0 & 0 \end{bmatrix}$$

$$\boldsymbol{A}_{23} = \begin{bmatrix} \multicolumn{2}{c}{\boldsymbol{O}_{5X2}} \\ -\frac{K_d}{I_6} & \frac{K_d}{I_6} \\ -\frac{(I_6+K_d)}{\tau_F I_6} & \frac{K_d}{\tau_F I_6} \\ 0 & -\frac{1}{\tau_F} \end{bmatrix}$$

$$\boldsymbol{B}_{CL} = \begin{bmatrix} \multicolumn{4}{c}{\boldsymbol{O}_{6X4}} \\ \frac{1}{I_1} & 0 & 0 & 0 \\ \multicolumn{4}{c}{\boldsymbol{O}_{4X4}} \\ 0 & \frac{K_i}{I_6} & \frac{K_p}{I_6} & 0 \\ 0 & \frac{K_i}{\tau_F I_6} & \frac{K_p}{\tau_F I_6} & 0 \\ 0 & 0 & 0 & \frac{1}{\tau_F} \end{bmatrix}$$

References

1. Schnabler, M., Stifter, C.: Model-Based Design Methods for the Development of Transmission Control Systems. In: Conference Paper, SAE International, 0148-7191 (2014)
2. Castiglione, M., Stecklein, G., Senseney, R., Stark, D.: Development of Transmission Hardware-in-the-Loop Test System. SAE Technical Paper, 2003-01-1027 (2003)
3. Bagalini, E.,Violante, M.: Development of an automated test system for ECU software validation: An industrial experience. In: 15th Biennial Baltic Electronics Conference (BEC), pp. 103–106, Tallinn, Estonia (2016)
4. Galvagno, E., Velardocchia, M., Vigliani, A., Tota, A.: Experimental Analysis and Model Validation of a Dual Mass Flywheel for Passenger Cars. SAE Technical Paper, 2015-01-1121 (2015)
5. Hwang, T., Roh, J., Park, K., Hwang, J., Lee, K.H., Lee, K., Lee, S.-J., Kim, Y.-J.: Development of HIL systems for active brake control systems. In: SICE-ICASE International Joint Conference (2006)
6. Lee, S.J., Kim, Y.J.: Development of hardware-in-the-loop simulation system for testing multiple ABS and TCS modules. Int. J. Veh. Des. **36**(1), 13–23 (2004)
7. Tota, A., Galvagno, E., Velardocchia, M., Vigliani, A.: Passenger car active braking system: Model and experimental validation (Part I). Proc. Inst. Mech. Eng. C J. Mech. Eng. Sci. **232**(4), 585–594 (2018)
8. Tota, A., Galvagno, E., Velardocchia, M., Vigliani, A.: Passenger car active braking system: Pressure control design and experimental results (part II). Proc. Inst. Mech. Eng. C J. Mech. Eng. Sci. **232**(5), 786–798 (2018)
9. Galvagno, E., Tota, A., Vigliani, A., Velardocchia, M.: Pressure following strategy for conventional braking control applied to a HIL test bench. SAE Int. J. Passenger Cars-Mech. Syst. **10**(2017-01-2496), 721–727 (2017)
10. Lee, M.H., et al.: Development of a hardware in the loop simulation system for electric power steering in vehicles. Int. J. Automot. Technol. **V12**, 733–744 (2011)
11. Galvagno, E., Tota, A., Velardocchia, M., Vigliani, A.: Enhancing Transmission NVH Performance through Powertrain Control Integration with Active Braking System. SAE Technical Paper 2017-01-1778 (2017)
12. Galvagno, E., Velardocchia, M., Vigliani, A.: Torsional oscillations in automotive transmission: Experimental analysis and modelling. Shock Vibration **2016** (2016)
13. Mendes, A., Meirelles, P.: Application of the hardware in-the-loop technique to an elastomeric torsional vibration damper. SAE Int. J. Engines **6**(4), 2004–2014 (2013)
14. Bracco, G., Giorcelli, E., Mattiazzo, G., Orlando, V., Raffero, M.: Hardware-in-the-loop test rig for the ISWEC wave energy system. Mechatronics **25**, 11–17 (2015)
15. Galvagno, E., Velardocchia, M., Vigliani, A.: Dynamic and kinematic model of a dual clutch transmission. Mech. Mach. Theory **46**(6), 794–805 (2011)
16. Leonhard, W.: Control of Electrical Drives. Springer Science & Business Media (2001)
17. Welch, P.D.: The use of fast Fourier transform for the estimation of power spectra: a method based on time averaging over short, modified periodograms. IEEE Trans. Audio Electroacoust. **15**(2), 70–73 (1967)
18. Guercioni, G.R., Galvagno, E., Tota, A., Vigliani, A., Zhao, T.: Driveline Backlash and Half-Shaft Torque Estimation for Electric Powertrains Control. SAE Technical Paper 2018-01-1345 (2018)
19. Osella, G., Cimmino, F., Galvagno, E., Vafidis, C., Velardocchia, M., Vigliani, A., Antonio, T.O.T.A.: U.S. Patent No. 10946855. U.S. Patent and Trademark Office, Washington, DC (2021)

Author Queries

Chapter 13

Query Refs.	Details Required	Author's response
AQ1	The closing parenthesis does not have a corresponding opening parenthesis in the caption of Fig. 4. Please insert the parenthesis in the appropriate position.	
AQ2	Caption of Figs. 10 and 14 seems to be identical. Please check and correct if necessary.	

MARKED PROOF

Please correct and return this set

Please use the proof correction marks shown below for all alterations and corrections. If you wish to return your proof by fax you should ensure that all amendments are written clearly in dark ink and are made well within the page margins.

Instruction to printer	*Textual mark*	*Marginal mark*
Leave unchanged	• • • under matter to remain	
Insert in text the matter indicated in the margin		New matter followed by or
Delete	/ through single character, rule or underline or through all characters to be deleted	or
Substitute character or substitute part of one or more word(s)	/ through letter or through characters	new character / or new characters /
Change to italics	— under matter to be changed	
Change to capitals	under matter to be changed	
Change to small capitals	under matter to be changed	
Change to bold type	under matter to be changed	
Change to bold italic	under matter to be changed	
Change to lower case	Encircle matter to be changed	
Change italic to upright type	(As above)	
Change bold to non-bold type	(As above)	
Insert 'superior' character	/ through character or where required	or under character e.g. or
Insert 'inferior' character	(As above)	over character e.g.
Insert full stop	(As above)	⊙
Insert comma	(As above)	,
Insert single quotation marks	(As above)	or and/or or
Insert double quotation marks	(As above)	or and/or or
Insert hyphen	(As above)	
Start new paragraph		
No new paragraph		
Transpose		
Close up	linking characters	
Insert or substitute space between characters or words	/ through character or where required	
Reduce space between characters or words	between characters or words affected	